



UNIVERSITÀ DEGLI
STUDI DI SALERNO



Facoltà di Ingegneria

Dipartimento di Ingegneria dell'Informazione ed Elettrica e
Matematica Applicata

Dottorato di Ricerca in Ingegneria dell'Informazione
XIV Ciclo – Nuova Serie

TESI DI DOTTORATO

Control Issues in Photovoltaic Power Converters

CANDIDATO: **MASSIMILIANO DE CRISTOFARO**

COORDINATORE: **PROF. MAURIZIO LONGO**

TUTOR: **PROF. NICOLA FEMIA**

CO-TUTOR: **PROF. GIOVANNI PETRONE**

Anno Accademico 2014 – 2015

**To my family
To my friends**

Contents

Contents 3

Introduction..... 5

Chapter 1 Photovoltaic Inverters..... 10

- 1.1 Half-Bridge Voltage Source Inverter..... 11
- 1.2 Full-Bridge Voltage Source Inverter 12
- 1.3 Three-phase Voltage Source Inverter 13
- 1.4 Neutral point Clamped Inverter 14
- 1.5 $\alpha\beta$ and dq transformations 16
- 1.6 Control techniques for PV inverters 20
- 1.7 Maximum Power Point Tracking techniques 25
- References..... 29

Chapter 2 An improved Dead-Beat control based on an Observe&Perturb algorithm..... 31

- 2.1 Description of the simulator tool 33
- 2.2 Standard controller design 35
 - 2.2.1 Proportional-Integral Linear Control design 38
 - 2.2.2 Dead-Beat control design 40
 - 2.2.3 Hybrid solution: Dead-Beat and integral action..... 45
- 2.3 Observe&Perturb Dead-Beat control..... 45
- 2.4 Simulation results 49
- 2.5 Implementation on a microcontroller 56
- References..... 61

Chapter 3 The Effect of a Constant Power Load on the Stability of a Smart Transformer65

- 3.1 Constant power load characteristic and single loop control analysis 68
- 3.2 Double loop control analysis 79
- References 82

Chapter 4 Minimum Computing MPPT84

- 4.1 Light-to-Light system case study 86
- 4.2 Adaptive duty-cycle setup 88
- 4.3 LED Dimming-based Bulk Voltage regulation 95
- 4.4 Experimental results 98
- References 107

Conclusions109**List of publications112****Acknowledgements113**

Introduction

The development of this thesis was born from cooperation between the *Power Electronics and Renewable Sources Laboratory* of the University of Salerno and the *ABB Solar Group* company (ex *Power-One*) of Terranuova Bracciolini (AR), Italy that is one of the most important manufactures of Photovoltaic (PV) power converters. Its portfolio covers all the possible PV systems: from the module (50-400W), to the string (0.2-2kW) up to the centralized solutions (more than 1MW).

This company has pointed out a great interest to investigate issues related to the control of PV systems to explore new control techniques that can have static and dynamic performance better than the existing techniques implemented in its systems, to analyze new scenarios due to the insertion of the Distributed Power Generating Systems (DPGSs) into the grid and to optimize the current methods to extract power from the PV source with the final goal to increase the performance of the PV systems at any level, system, grid and circuit. Specifically the progress of photovoltaic technology has opened a scenario of different solutions:

- at system level, still today there is a high interest of the industry for the centralized solutions in less-developing country, such as China, India and Thailand, where the system must work in poor grid conditions with great changes of frequency and root-means square value and must be able to ensure the respect of the regulation requirements during the grid faults. So, define new current control techniques that allow having better performance for these systems is currently a challenge for the industry;
- at grid level, it has enabled a transition from a highly centralized structure of electric power system, with large capacity generators, to a new decentralized infrastructure with the insertion of small and medium capacity generators. This has led great changes in the electric grid. The conventional

grid was composed of a source, a distribution energy system and loads. Instead, new scenarios include the presence of DPGSs that can inject locally energy into the grid. The study of DPGSs is of a great interest from the point of view of the overall system, where it is important to choice where it is convenient to insert the DPGS, as well as from the point of view of the local system, where there are problems to control and synchronization. Moreover, the increase in performance, combined with the costs reduction of solid state devices, has led to the development and the diffusion of the power converters with the result that, today, almost the totality of the electrical energy is controlled by power electronic systems;

- at circuit level, the wide interest for Maximum Power Point Tracking (MPPT) control is justified by the attempt to maximize the energy harvested from photovoltaic sources in all the operating conditions. Several control techniques can be adopted, both analog and digital, to achieve good MPPT efficiency. Digital techniques are best suited to implement adaptive control. The runtime optimization of MPPT digital control is in the focus of many studies, mostly regarding the Perturb&Observe (P&O) technique. The two parameters determining the MPPT efficiency and the tracking speed P&O technique are the sampling period T_{MPPT} and the duty-cycle step perturbation magnitude ΔD . The level of MPPT efficiency achievable by the most of the existing techniques is conditioned by many factors, such as the modeling assumptions, the duty-cycle and sampling period correction law adopted, the computing capabilities of the digital device adopted for the control implementation. To this regard, they involve a variable amount of computations, including the calculation of the ratios (e.g. $\Delta I/\Delta D$, $\Delta P/\Delta V$) used as figure of merit, the subsequent calculations required by the adaptation law, and the additional calculations required by specific estimation/decision algorithm used. As a consequence, many methods and algorithms yield high MPPT efficiency at the price of high computing effort, which is not compatible with low cost requirements. Achieving maximum energy harvesting

with minimum cost devices is a fundamental renewable energy industry demand.

Hence, there are many issues, also attractive for the scientific field, to investigate about the design of PV systems in the present-day evolving scenario, as it is not completely defined. For this reason, during this study, models, methods and algorithms will be developed to analyze these challenges at any level starting from the inputs provided by *ABB Solar Group*.

The dissertation is organized as follows.

In the chapter 1, the basic circuit topologies and tools used for the PV systems will be presented. The main aim is to explain the operation of circuits and tools used by *ABB Solar Group* for its converters and that will be used for the control issues analyzed in the next chapters. Hence, the basic Voltage Source Inverter (VSI), single-phase and three-phase, and the multilevel Neutral Point Clamped (NPC) inverter will be discussed. Also very useful tools for the control design, the $\alpha\beta$ and dq transformations, will be summarized and, at the end, an overview of the existing control and MPPT techniques will be presented.

In the chapter 2, an improved Dead-Beat control based on an Observe&Perturb (O&P) algorithm will be developed for the Neutral Point Clamped (NPC) inverter that is the most widely used topology of multilevel inverters for high power applications. Indeed a NPC-based inverter, the *AURORA ULTRA* of 1.4MW, is developed by *ABB Solar Group* mainly for the Asian market. A comprehensive comparison between the standard Dead-Beat, the proportional-integral and the proposed Dead-Beat control will be performed for a passive NPC inverter. Also stability aspects for these controllers will be analyzed and, based on that, the general guideline to select the parameters of the proposed O&P algorithm will be defined. The comparison will be done with a dedicated simulation tool, written in C++ language, since the existing commercial software, such as Simulink[®], PSIM[®] and PSPICE[®], allow to make the analysis only a specific level: system, circuit or device. Both O&P method and simulation tool are not only for NPC inverters but they are very

general being able to be applied to all the converters. At the end, the proposed O&P Dead-Beat control will be implemented on a TMS320F28379D Dual-Core Delfino™ Microcontroller (μc) to test the feasibility of all its components in a single embedded system. The choice of the F28379D μc is carried out to use the same family, the TI C2000, that *ABB Solar Group* implements on its converters and to have the best performance with a dual-core system. This μc implementation has been performed at the Texas Instruments of Freising, Germany.

In the chapter 3, a critical scenario for the stability of the electric grid will be investigated. It will be implemented with a Smart Transformer (ST) that can be composed by one or more energy conversion stages, i.e. one or more power converters, some loads and some DPGSs directly connected to the low voltage side of the ST. The ST is a Solid State Transformer (SST) used in electric distribution system to provide ac bus voltages with a fixed amplitude and frequency for each of the possible configuration of loads. The international industry practice on load modeling for static and dynamic power system studies will be discussed and it will be shown that the Constant Power Load (CPL) model is mostly used (about 84%) for power system static analysis. The main characteristic of a CPL is that its current decreases when its voltage increases and vice versa and, so, it presents negative impedance for the small signal analysis that can impact the system stability. For this reason, in this chapter, the scenario with only CPLs, the worst case for the stability, will be analyzed to verify if it is possible to use controllers usually designed for stable systems even when the CPLs make the system unstable. A three-phase system, composed by a Voltage Source Inverter (VSI) with an LC filter representing the output stage of the ST, a DC-source that represents the ST DC bulk, the CPL, the controller and the Pulse Width Modulator (PWM) will be considered. At the end the conditions to design the LC filter to have a stable system with a CPL will be provided. The analysis of a system with a CPL has been developed also in cooperation with the *Chair of Power Electronics* of the Albrechts-Universität zu Kiel, Germany.

In the chapter 4, after that the methodologies to track the Maximum Power Point (MPP) will be presented, a method to

determine the sampling period T_{MPPT} and the duty-cycle step perturbation magnitude ΔD will be developed. This realizes the real time adaptation of a photovoltaic P&O MPPT control with minimum computing effort to maximize the PV energy harvesting against changes of sun irradiation, the temperature and the characteristics of the PV source and by the overall system the PV source is part of. It exploits the correlation existing among the MPPT efficiency and the onset of a permanent 3 level quantized oscillation around the MPP. A comparison between an existing adaptive MPPT algorithm will be performed through simulations, to set exactly the same test conditions and, after, as a multifunction control application case study, a TMS320F28035 Texas Instruments Piccolo™ Microcontroller will be used to implement the proposed adaptive PV MPPT control algorithm on a 70W LED lighting system prototype fed by a photovoltaic source, with a capacitor working as storage device. The choice of the F28035 μc is carried out to use the same family, the TI C2000, that *ABB Solar Group* implements on its converters but with a single-core system as the goal of the proposed method is the minimum computing effort. Hence the aim of this chapter is to determine an optimize MPPT algorithm that can be implemented in the *ABB Solar Group* systems.

Chapter 1

Photovoltaic Inverters

The PV inverter is the main element of grid-connected PV power systems: it converts the power from the PV source into the AC grids. The development of the circuit topologies for the PV inverters has had as principal goal to maximize the efficiency but other complex functions, usually not present in motor drive inverters, are typically required like the maximum power point tracking, anti-islanding and grid synchronization [1]. To have an increment of the efficiency, the galvanic isolation typically provides by high-frequency transformers in the DC/DC boost converter or by a low-frequency transformer on the output has been eliminated. But the transformerless structure typically requires more complex solutions to keep the leakage current and DC current injection under control in order to comply with the safety issues resulting in novel topologies. These topologies have been taking the starting point from two converter families: H-bridge and Neutral Point Clamped (NPC) that are the most suitable respectively for low power inverter (up to tens of kW) and for high power inverters (hundreds of kW) [1].

The aim of this chapter is to explain the operation of the basic circuits, H-bridge and NPC, and to introduce very useful tools for the control design of these inverters, the $\alpha\beta$ and dq transformations. Also, at the end, an overview of the existing control and Maximum Power Point Tracking (MPPT) techniques is presented.

These circuits, tools and control techniques, all used by *ABB Solar Group* in its converts, represent the starting points for the control issues addressed in the next chapters.

1.1 Half-Bridge Voltage Source Inverter

The figure 1.1 shows the power topology of a half-bridge VSI [2], where two capacitors (C_+ and C_-) are required to provide a neutral point N, such that each capacitor maintains a constant voltage $v_i/2$. Because the current harmonics injected by the operation of the inverter are low-order harmonics, a set of large capacitors is required.

It is clear that both switches S_+ and S_- cannot be ON simultaneously because a short circuit across the dc link voltage source v_i would be produced. There are two defined (states 1 and 2) and one undefined (state 3) switch states as shown in the table 1.1. In order to avoid the short circuit across the dc bus and the undefined ac output voltage condition, the modulating technique should always ensure that at any instant either the top or the bottom switch of the inverter leg is ON [3].

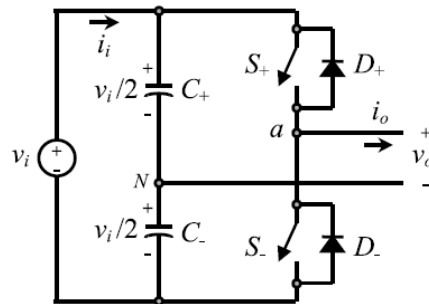


Fig 1.1 Single-phase half bridge VSI

State	v_o	Components Conducting
S_+ is ON and S_- is OFF	$v_i/2$	S_+ if $i_o > 0$ D_+ if $i_o < 0$
S_- is ON and S_+ is OFF	$-v_i/2$	S_- if $i_o > 0$ D_- if $i_o < 0$
S_+ and S_- are all OFF	$v_i/2$ $-v_i/2$	D_+ if $i_o > 0$ D_- if $i_o < 0$

Table 1.1 Switch states for a half-bridge single-phase VSI

1.2 Full-Bridge Voltage Source Inverter

The figure 1.2 shows the power topology of a full-bridge VSI [2]. This inverter is similar to the half-bridge inverter but a second leg provides the neutral point N to the load. Both switches S_{1+} and S_{1-} (or S_{2+} and S_{2-}) cannot be ON simultaneously because a short circuit across the dc link voltage source v_i would be produced. The table 1.2 shows the possible five states of this circuit: four defined and one undefined.

The modulation technique, ensuring that either the top or the bottom switch of each leg is ON at any instant, avoids the short circuit across the dc bus and the undefined ac output voltage condition. Looking at the tables 1.2 and 1.1, it is possible to notice that the ac output voltage for the full-bridge can take values up to the dc link value v_i , while the half-bridge can reach $v_i/2$. [3].

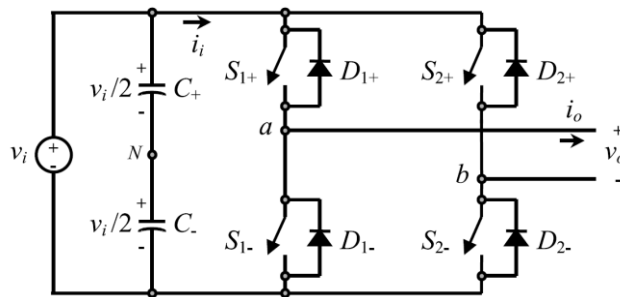


Fig 1.2 Single-phase full bridge VSI

State	v_a	v_b	v_o	Components Conducting
S_{1+} and S_{2-} are ON and S_{1-} and S_{2+} are OFF	$v_i/2$	$-v_i/2$	v_i	S_{1+} and S_{2-} if $i_o > 0$ D_{1+} and D_{2-} if $i_o < 0$
S_{1-} and S_{2+} are ON and S_{1+} and S_{2-} are OFF	$-v_i/2$	$v_i/2$	$-v_i$	S_{1-} and S_{2+} if $i_o > 0$ D_{1-} and D_{2+} if $i_o < 0$
S_{1+} and S_{2+} are ON and S_{1-} and S_{2-} are OFF	$v_i/2$	$v_i/2$	0	S_{1+} and S_{2+} if $i_o > 0$ D_{1+} and D_{2+} if $i_o < 0$
S_{1-} and S_{2-} are ON and S_{1+} and S_{2+} are OFF	$-v_i/2$	$-v_i/2$	0	S_{1-} and S_{2-} if $i_o > 0$ D_{1-} and D_{2-} if $i_o < 0$
S_{1+} , S_{2+} , S_{1-} and S_{2-} are all OFF	$-v_i/2$ $v_i/2$	$v_i/2$ $-v_i/2$	$-v_i$ v_i	D_{1-} and D_{2+} if $i_o > 0$ D_{1+} and D_{2-} if $i_o < 0$

Table 1.2 Switch states for a full-bridge single-phase VSI

1.3 Three-phase Voltage Source Inverter

The single-phase VSIs cover low-range power applications while the three-phase VSIs cover the medium to high-power applications (from few hundreds of kW) [2]. The main purpose of these topologies is to provide a three-phase voltage source, where the amplitude, phase, and frequency of the voltages should always be controllable. Although most of the applications require sinusoidal voltage waveforms, arbitrary voltages are also required in some emerging applications (e.g. active filters, voltage compensators).

The standard three-phase VSI topology is shown in the figure 1.3 and the eight valid switch states are given in the table 1.3 based on the same considerations for the single-phase VSIs described in the previous sections. Of the eight valid states, two of them (7 and 8 in the table 1.3) produce zero ac line voltages. In this case, the ac line currents freewheel through either the upper or lower components. The remaining states (1 to 6 in table 1.3) produce no-zero ac output voltages. In order to generate a given voltage waveform, the inverter moves from one state to another. Thus the resulting ac output line voltages consist of discrete values of voltages that are v_i , 0, and $-v_i$ for the topology considered. [3].

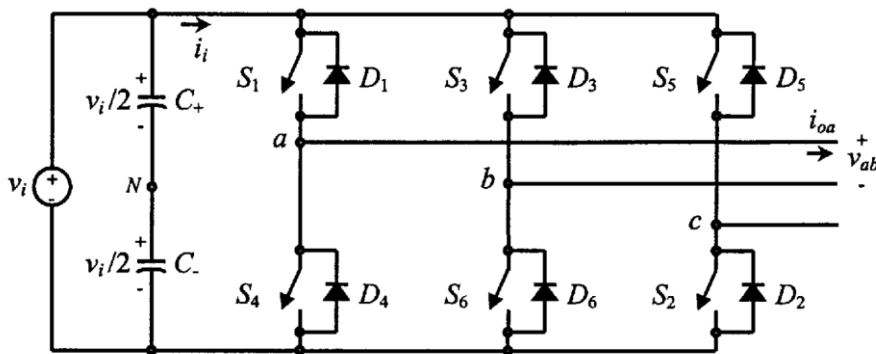


Fig 1.3 Three-phase VSI

State	v_{ab}	v_b	v_a
1. S_1, S_2 and S_6 are ON and S_4, S_5 and S_3 are OFF	v_i	0	$-v_i$
2. S_2, S_3 and S_1 are ON and S_5, S_6 and S_4 are OFF	0	v_i	$-v_i$
3. S_3, S_4 and S_2 are ON and S_6, S_1 and S_5 are OFF	$-v_i$	v_i	0
4. S_4, S_5 and S_3 are ON and S_1, S_2 and S_6 are OFF	$-v_i$	0	v_i
5. S_5, S_6 and S_4 are ON and S_2, S_3 and S_1 are OFF	0	$-v_i$	v_i
6. S_6, S_1 and S_5 are ON and S_3, S_4 and S_2 are OFF	v_i	$-v_i$	0
7. S_1, S_3 and S_5 are ON and S_4, S_6 and S_2 are OFF	0	0	0
8. S_4, S_6 and S_2 are ON and S_1, S_3 and S_5 are OFF	0	0	0

Table 1.3 Valid switch states for a three-phase VSI

1.4 Neutral point Clamped Inverter

The multilevel inverter has been developed to improve the performance of the two levels inverters and has become more and more interesting with the continuous evolution of the power switches in term of voltage and current rating and price [3].

A multilevel inverter that has the same voltages and powers of a two levels inverter has a better voltages harmonic spectrum so it is simpler to respect the law requirements. Indeed, having more levels, it is able to reproduce voltage and current waveforms more similar to a sinusoidal one and so the load absorbs fewer harmonic.

The principal effects of the harmonic reductions into the current loads are:

- less power losses in the iron and copper
- less electromagnetic interferences (EMIs)
- less mechanical oscillations in motor loads

The Neutral Point Clamped (NPC) inverter is the most extensively applied multilevel converter topology at present [3]. A three-level NPC inverter is illustrated in the figure 1.4, which is able to provide five-level-step-shaped line to line voltage (three-level-step-shaped phase voltage) without transformers or reactors and so it can reduce harmonics in both of the output voltage and current. The main benefit of this configuration is that each of the switches must block only half

of the dc-link voltage V_{dc} even if their number is twice of a two-level inverter. However, the NPC inverter has some drawbacks, such as additional clamping diodes, a complex Pulse Width Modulation (PWM) switching pattern design and a possible deviation of Neutral Point (NP) voltage. In addition, since the NPC inverter is mostly used for medium or high-power applications, the minimization of the switching losses is such a relevant issue. As to the modulation strategies, three popular modulation techniques for NPC inverters, Carrier-Based (CB) PWM, Space Vector Modulation (SVM) and Selective Harmonic Elimination (SHE), have been widely used in practice. The SHE method shows an advantage for high-power applications due to having a small number of switching actions. The other two PWM techniques are commonly used in various applications because of their high PWM qualities [3].

A leg of a three-level NPC inverter is shown in the figure 1.4 where it is possible to note the structural differences compared to the two-level inverter. A three-level NPC inverter has 4 switches (S_{a1} , S_{a2} , S_{a3} , S_{a4}) and other 2 diodes (D_{ca1} , D_{ca2}) with the function to clamp the output voltage as they are connected to the medium point of the DC bus between two equal capacitors. Hence, the possible V_{ao} values are $V_{dc}/2$ and $-V_{dc}/2$. The table 1.4 shows the switches states with a fixed output voltage. It is worth noting that the control signal of S_{a1} is in opposite phase of S_{a3} as well as the signal control of S_{a2} is in opposite phase of S_{a4} . The four switches cannot be ON or OFF at the same time for the same reasons of the two-level inverters [4].

Three inverter legs in parallel can work independently making in the output the three sinusoidal voltages with 120 degrees of phase shift. In this topology, the reverse maximum voltage of the switches is $V_{dc}/2$ while for two-level it is V_{dc} . This leads to select cheaper switches than for the two-level inverter even if the number is greater.

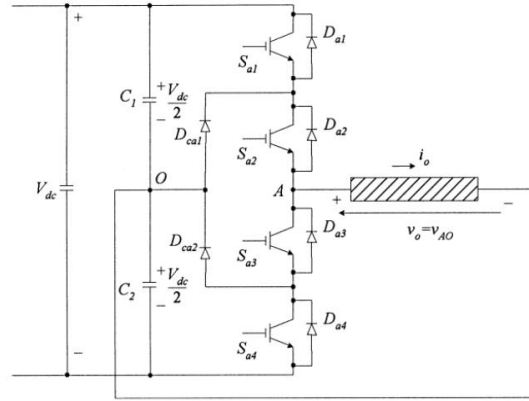


Fig 1.4 Multilevel Neutral Point Clamped Inverter

State	v_{AO}	Components Conducting
S_{a1}, S_{a2} are ON and S_{a3} and S_{a4} are OFF	$V_{dc}/2$	S_{a1}, S_{a2} if $i_o > 0$ D_{a1}, D_{a2} if $i_o < 0$
S_{a2}, S_{a3} are ON and S_{a1} and S_{a4} are OFF	0	D_{ca1}, S_{a2} if $i_o > 0$ D_{ca2}, S_{a3} if $i_o < 0$
S_{a3}, S_{a4} are ON and S_{a1} and S_{a2} are OFF	$-V_{dc}/2$	D_{a3}, D_{a4} if $i_o > 0$ S_{a3}, S_{a4} if $i_o < 0$

Table 1.4 Switch states for a NPC inverter

1.5 $\alpha\beta$ and dq transformations

When the three phase converter is characterized by four wires, i.e. three phases plus neutral, the application is straightforward since a four-wire three-phase system is totally equivalent to three independent single-phase systems [5]. In contrast, it would need to apply more caution when it is dealing with a three-phase system with an insulated neutral, i.e. with a three-wire three-phase system. The aim of this section is to give the basic knowledge needed to extend the control principles to this kind of systems. Two fundamental tools are required to design an efficient three-phase controller: the $\alpha\beta$ transformation and the dq transformation.

The $\alpha\beta$ transformation represents a very useful tool for the analysis and modeling of three-phase electrical systems. In general, a three-phase linear electric system can be properly described in mathematical terms only by writing a set of tridimensional dynamic equations (integral and/or differential), providing a self-consistent

mathematical model for each phase. In some cases though, the existence of physical constraints makes the three models not independent from each other. In these circumstances the order of the mathematical model can be reduced, from three to two dimensions, without any loss of information. As it is meaningful to reduce the order of the mathematical model, the $\alpha\beta$ transformation represents the most commonly used relation to perform this reduction [5].

Considering a tridimensional vector $x_{abc} = [x_a \ x_b \ x_c]^T$ that can be any triplet of the system electrical variables, voltages or currents, it is possible to introduce the linear transformation, $T_{\alpha\beta\gamma}$:

$$\begin{bmatrix} x_\alpha \\ x_\beta \\ x_\gamma \end{bmatrix} = T_{\alpha\beta\gamma} \begin{bmatrix} x_a \\ x_b \\ x_c \end{bmatrix} = \sqrt{\frac{2}{3}} \begin{bmatrix} 1 & -1/2 & -1/2 \\ 0 & \sqrt{3}/2 & -\sqrt{3}/2 \\ 1/\sqrt{2} & 1/\sqrt{2} & 1/\sqrt{2} \end{bmatrix} \begin{bmatrix} x_a \\ x_b \\ x_c \end{bmatrix} \quad (1.1)$$

which, in geometrical terms, represents a change from the set of reference axes denoted as abc to the equivalent one indicated as $\alpha\beta\gamma$.

The $T_{\alpha\beta\gamma}$ transformation has the following interesting property:

$$x_a + x_b + x_c = 0 \Rightarrow x_\gamma = 0 \quad (1.2)$$

Every time the constraint (1.2) is valid for a tridimensional system, the coordinate transformation $T_{\alpha\beta\gamma}$ allows describing the same system in a bidimensional space without any loss of information.

Considering a triplet of symmetric sinusoidal signals:

$$\begin{aligned} e_a &= U_M \sin(\omega t) \\ e_b &= U_M \sin(\omega t - 2\pi/3) \\ e_c &= U_M \sin(\omega t + 2\pi/3) \end{aligned} \quad (1.3)$$

it is easy to verify that

$$\begin{aligned}
 e_\alpha &= \sqrt{\frac{2}{3}} U_M \sin(\omega t) \\
 e_\beta &= \sqrt{\frac{2}{3}} U_M \cos(\omega t)
 \end{aligned}
 \tag{1.4}$$

and that the space vector, e_{abc} , associated with (1.3), satisfies the constrain (1.2) and so it can be described without loss of information in the $\alpha\beta$ reference frame.

Hence the three-phase inverter is completely equivalent to a couple of independent single-phase inverters making the controller design of such inverter possible in the $\alpha\beta$ reference frame and leading to an improvement of the performance as it will be shown in the chapter 4 of this work.

Another useful tool is the dq transformation that exploits the Park transform, a very well-known tool for electrical machine designers. While the $\alpha\beta$ transformation maps the three-phase inverter and its load onto a fixed two-axis reference frame, the dq transformation maps them onto a two-axis synchronous rotating reference frame. This practically means moving from a static coordinate transformation to a dynamic one, i.e. to a linear transformation whose matrix has time varying coefficients.

The transformation defines a new set of reference axes, called d and q , which rotate around the static $\alpha\beta$ reference frame at a constant angular frequency ω . The rotating vector angular speed equals the angular frequency of the original voltage triplet, which it is possible to consider the fundamental frequency of the three-phase system. If the angular speed of the rotating vector equals ω in the dq reference frame, the vector is not moving at all. Hence, the advantage is represented exactly by the fact that sinusoidal signals with angular frequency ω are seen as constant signals in the dq reference frame. This principle is exploited in the implementation of the so-called synchronous frame current control in the chapter 2, where the Park transform angular speed is chosen exactly equal to the three-phase system fundamental frequency.

The following matrix provides the mathematical formulation of the Park transform considering the equation (1.1):

$$\begin{bmatrix} x_d \\ x_q \end{bmatrix} = T_{dq} \begin{bmatrix} x_\alpha \\ x_\beta \end{bmatrix} = \begin{bmatrix} \cos \theta & \sin \theta \\ -\sin \theta & \cos \theta \end{bmatrix} \begin{bmatrix} x_\alpha \\ x_\beta \end{bmatrix} \quad (1.5)$$

The two system dynamic equations are complicated by the cross-coupling of the two axes, i.e. they are no longer independent from each other. This is the reason why, decoupling feed-forward paths are usually included in the control scheme making the system dynamic totally identical to those of the original one.

To complete the discussion of the Park transform, it worth be noted that it is also possible to implement the so-called inverse sequence Park transform where the direction of the dq axes rotation is assumed to be inverted, while the transformation (1.5) can be identified as the direct sequence Park transform. This inverse transformation could be required when the system is unbalanced and asymmetrical as impedance unbalances and/or asymmetric voltage sources can be found. In this case, a three-phase system can be shown to be equivalent to the superposition of a direct sequence system and an inverse sequence system, both of them symmetrical and balanced and so both properly describable in the this reference.

Also, because the elements of T_{dq} are not time invariant, the application of the Park transform, differently from the $\alpha\beta$ transformation, affects the system dynamics: any controller, designed in the dq reference frame, is actually equivalent to a stationary frame controller that does not maintain the same frequency response.

1.6 Control techniques for PV inverters

In the figure 1.5, the schematic grid-connected system representation is shown while the current control loop is considered in the figure 1.6 in order to analyze the error caused by the control of AC quantities in steady-state condition.

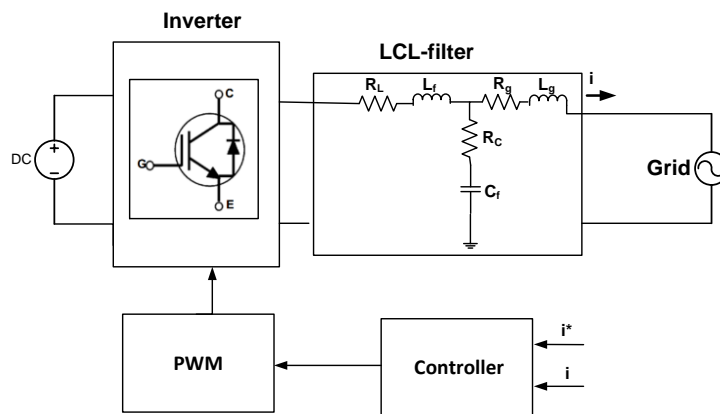


Fig 1.5 Schematic grid-connected system representation

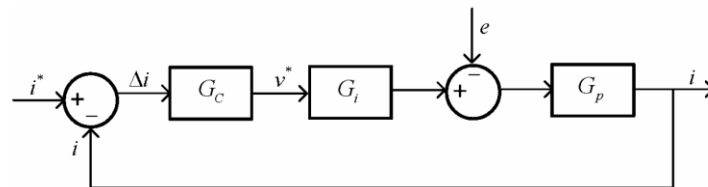


Fig 1.6 Current Control Loop

The variables shown in the figure 1.6 are as follows:

- e is grid voltage acting on the system as a perturbation
- i^* is the current reference for the current control loop
- i is the measured grid current
- Δi is the error between the measured grid current and the current reference
- G_c is controller transfer function in the Laplace domain
- G_i is the inverter transfer function in the Laplace domain

- G_p is the plant transfer function in the Laplace domain, which is usually composed by the output filter of the converter and the grid impedance
- v^* is the controller output voltage

It has been demonstrated [6] that the grid connected LCL filter can be regarded as an inductance for low frequencies. So it is possible to define:

$$G_p(s) = \frac{1}{Ls + R} \quad (1.6)$$

where L and R are respectively the filter inductance and its parasitic resistance.

Indicating T_s the sampling time of a typical digital system, G_i is the delay due to elaboration of the computation device (typically $1T_s$) and to the PWM (typically $0.5T_s$) [1]:

$$G_i(s) = \frac{1}{1.5T_s s + 1} \quad (1.7)$$

Hence, the current error produced by the perturbations e is:

$$\Delta_i(s) = \frac{G_p(s)}{1 + G_c(s)G_i(s)G_p(s)} e(s) \quad (1.8)$$

The controller goal is to minimize the steady-state current error $\Delta i(s)$.

There are several strategies for the control of the AC current in the case of Distributed Power Generation Systems (DPGSs). A very common technique used for three-phase systems is the dq control, synchronous rotating dq reference frame based on the dq transformation introduced in the former section. This technique is currently used by *ABB Solar Group* for its three-phase inverters. However, the dq control strategy cannot be implemented for a single-phase system [1] unless an imaginary circuit is coupled to the real one to simulate a two-axis environment [7]. Several controllers, such as PI, Resonant and Dead-Beat, can be considered in order to control the

current in the case of DPGSs. In the situation when the control strategy is implemented in the stationary reference frame, the use of the classical PI control leads to unsatisfactory current regulation since the PI control are designed in order to control DC quantities which are present only in the rotating reference frame [1].

The PI current controller G_{PI} is defined as:

$$G_{PI}(s) = k_p + \frac{k_I}{s} \quad (1.9)$$

It provides a finite gain corresponding to the grid voltage frequency. Hence, an improvement is to introduce a feedforward of the voltage (e_{ff} in the figure 1.7) to reduce the steady-state error of the PI controller and to increase the dynamic response. The figure 1.7 shows the block diagram with this variation. The voltage feed-forward signal is obtained by filtering the measured voltage; otherwise the use of the voltage feed-forward can lead to stability problems related to the delay introduced in the system by the voltage filter. Besides, the feed-forward compensation reduces the error due to the grid disturbance but cannot eliminate the steady-state error since its elimination is possible only by using a controller able to track a sinusoidal reference.

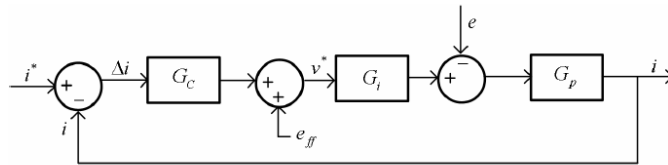


Fig 1.7 Current control loop with a PI controller

Since PI controller for an AC current exhibits two drawbacks [1]:

- high steady-state amplitude and phase errors
- poor disturbance rejection capability

the result is a non-compliance with international standards. For a typical grid-inverter the current controller should be able to track the waveform of the current reference and to eliminate the effects of the grid disturbances. For these reasons, in the chapter 2, a Dead-Beat

technique based on an Observe&Perturb algorithm will be presented and the design of the Dead-Beat control will be discuss in detail.

Another technique, the Resonant control, includes in the controller a model of the reference signal and external disturbances so robust tracking and disturbances rejection are achieved, as stated by the Internal Model Principle (IMP) [8].

In the hypothesis of neglecting the grid voltage harmonics, the grid voltage e can be defined as:

$$e(s) = \frac{N_E(s)}{D_E(s)} = k \frac{\omega}{s^2 + \omega^2} \quad (1.10)$$

where N_E and D_E are the numerator and denominator of e and k is the grid voltage amplitude. Including D_E in the generic form of the controller G_c :

$$G_c(s) = \frac{N_c(s)}{D_c(s)D_E(s)} \quad (1.11)$$

it results that the expression of the error Δi produced by the perturbation e , equation (1.5), can be expressed as:

$$\Delta_i(s) = \frac{N_p(s)D_c(s)D_i(s)N_E(s)}{D_p(s)D_c(s)D_i(s)D_E(s) + N_p(s)N_c(s)N_i(s)} \quad (1.12)$$

where N_p and D_p are the numerator and denominator of G_p and N_c and D_c are the numerator and denominator of G_c . If N_c and D_c are able to ensure that the overall system is stable, it can be seen that $\Delta i(t)$ converges to zero when $t \rightarrow \infty$.

Hence, the P+Resonant regulator is defined as:

$$C_{PRes}(s) = k_p + k_i \frac{s}{s^2 + \omega^2} \quad (1.13)$$

where k_p and k_i are the proportional and resonant gain and $s/(s^2+1)$ is the generalized integrator (GI). k_p is tuned in order to ensure that the overall system has a specific second-order response in terms of rise time, settling time and maximum overshoot since the size of the proportional gain k_p determines the bandwidth and the stability margins [1], [9], [10], in the same way as in the PI controller.

In the figure 1.8 the effect of k_i is shown through the bode plot of C_{Pres} for $k_p=1$, $\omega=2\pi 50\text{rad/s}$ and $k_i=1, 10$ and 100 rad/s. As it is possible to note, C_{Pres} behaves as a band-pass filter centered at the resonance frequency that it is equal to the grid frequency and k_i determines the bandwidth centered at the resonance frequency where the attenuation is positive. Hence k_i is usually tuned in order to obtain sufficient attenuation of the tracking error in case of grid frequency changes [1].

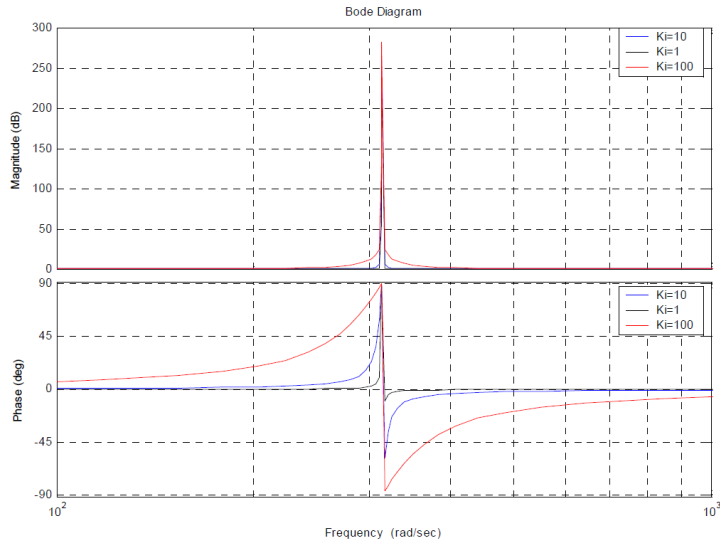


Fig 1.8 Bode plot of C_{Pres} with $k_i=1, 10, 100$ rad/s

Considering the P+Resonant controller and applying the final value theorem, the equation (1.14) is obtained:

$$\lim_{s \rightarrow 0} s \frac{k\omega(s^2 + \omega^2)(0.5Ts + 1)}{(Ls + R)(s^2 + \omega^2)(0.5Ts + 1) + (k_p s^2 + k_I s + k_p \omega^2)} = 0 \quad (1.14)$$

Hence, it can be proven that, with $e(s)=0$, $\Delta i(t)$ converges to zero when $t \rightarrow \infty$. The GI achieves an infinite gain at the resonant frequency, so the current reference tracking is ensured setting the resonant frequency of the controller to the fundamental frequency [11-13].

The P+Resonant controller will be used in the chapter 3 to analyze a critical scenario for the stability of the electric grid with a constant power load (CPL).

1.7 Maximum Power Point Tracking techniques

The maximum power point tracking (MPPT) control can be achieved with a number of different techniques, each one differing from the other for complexity, robustness, static and dynamic performance. To compare the different techniques it is possible to use the efficiency that can be defined as “the ratio between the energy extracted from the output terminals of a photovoltaic field and the energy really available” [14]. The available power depends on the solar irradiation while the extracted power depends on the impedance matching between source and load.

The Perturb and Observe (P&O) is the most widespread technique thanks to its simplicity and cost-effectiveness and also *ABB Solar Group* usually implements this technique in its converters. It implements a fixed-step hill climbing technique and, in the basic version, a fixed-amplitude perturbation of the duty-cycle (ΔD) is introduced by the controller at a fixed time step T_a . Varying the converter duty cycle the system operation point changes and consequently the output power extracted by the photovoltaic source. In order to calculate the actual output power $P[kT_a]$, it is necessary to measure the voltage and the current of the panel. This power is compared to the value obtained from the last measurement $P[(k-1)T_a]$. If $(P[kT_a]-P[(k-1)T_a])$ is positive, the controller keeps changing the duty cycle in the same direction. When $(P[kT_a]- P[(k-1)T_a])$ is

negative the duty cycle change is reversed. The control algorithm can be summarized by the following equation [15]:

$$D_{(k+1)T_a} = D_{kT_a} + (D_{kT_a} - D_{(k-1)T_a}) \text{sign}(P_{kT_a} - P_{(k-1)T_a}) \quad (1.15)$$

With this algorithm, once reached the maximum power point, the system operating point will swing around it. This causes a power loss that depends on the perturbation amplitude ΔD . If ΔD is large, the MPPT algorithm responds faster to sudden changes in operating conditions, with the trade-off of increasing the losses under stable or slowly changing conditions. If ΔD is small, the losses under stable or slowly changing conditions are reduced but the system has a slower response to rapid changes in temperature or irradiance level [14]. The P&O algorithm is explained by the flowchart in the figure 1.9.

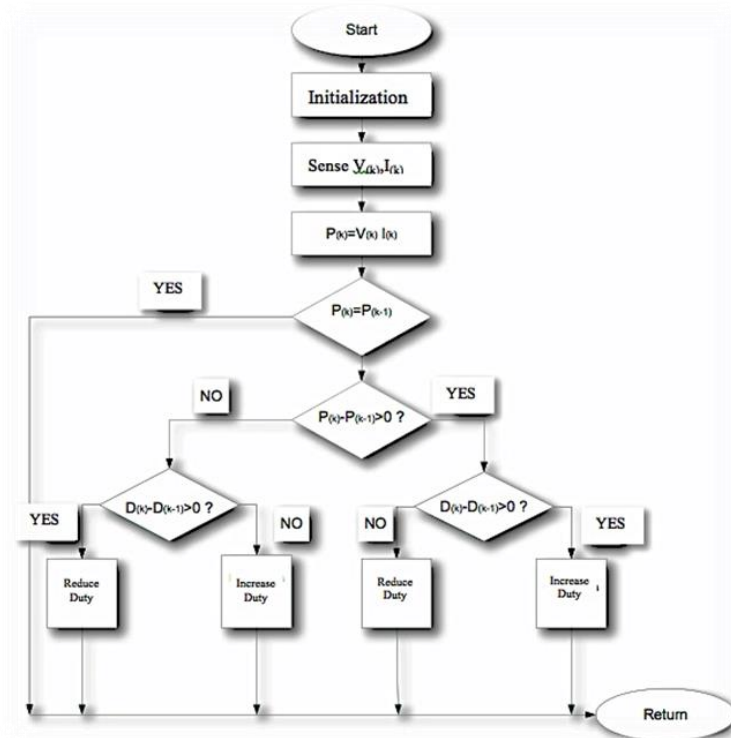


Fig 1.9 P&O algorithm flowchart

Another very used technique, the Incremental Conductance (IC) MPPT algorithm is based on the fact that the derivative of the output power (P) respect to the panel voltage (V) is equal to zero at the maximum power point. This derivative is greater than zero on the left of the MPP and lower than zero on the right of the MPP:

$$\frac{dP}{dV} = 0 \text{ for } V = V_{MPP} \quad (1.16)$$

$$\frac{dP}{dV} < 0 \text{ for } V < V_{MPP} \quad (1.17)$$

$$\frac{dP}{dV} > 0 \text{ for } V > V_{MPP} \quad (1.18)$$

Since $P=VI$, where I is the panel current:

$$\frac{dP}{dV} = \frac{d(VI)}{dV} = I \frac{dV}{dV} + V \frac{dI}{dV} = I + V \frac{dI}{dV} \quad (1.19)$$

From the equations (1.16) and (1.19):

$$\frac{dI}{dV} = -\frac{I}{V} \quad (1.20)$$

Where dI/dV is the incremental conductance and I/V is the instantaneous conductance. This algorithm changes the system operating point, step by step, until the instantaneous conductance and the incremental conductance are approximately equal. In this operating point, the photovoltaic system reaches the maximum output power. Also in this case, as in the P&O algorithm, the key features are the amplitude and frequency of the perturbation [14]. A flowchart of this algorithm is depicted in the figure 1.10.

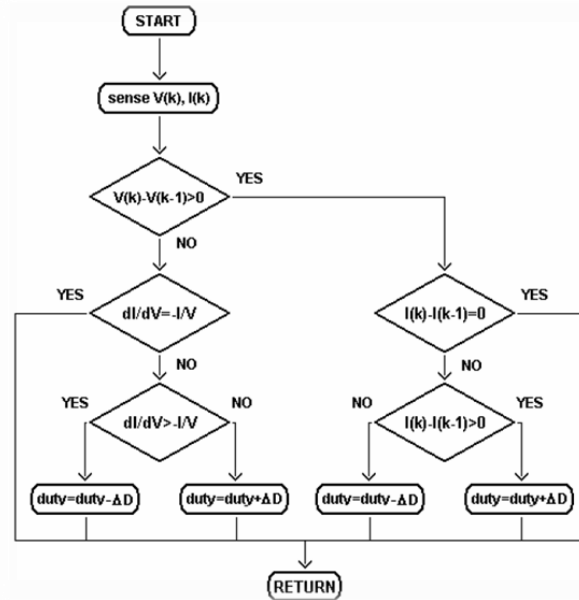


Fig. 1.10 Incremental conductance algorithm flowchart

The advantage of the IC technique, respect to the P&O, is that the difference between the incremental conductance and the instantaneous conductance gives a direct knowledge of the distance between the operating point and the maximum power point. Therefore, exploiting this property, an amplitude variation of the perturbation can be realized, so that the controller uses a large perturbation step when the operating point is far from the MPP and reduces the perturbation amplitude to a minimum value once MPP is reached. In this way the algorithm is much more efficient in comparison to a classic IC algorithm. The disadvantages are the more complex computing compared to the P&O.

The industry interest is to use very cheap computer and, so, an adaptive P&O technique with minimum computing effort will be implemented in the chapter 4.

References

- [1] Teodorescu R., Liserre M., Rodriguez P., "Grid Converters for Photovoltaic and Wind Power System", IEEE Press, WILEY
- [2] Ned Mohan, Tore M. Undeland, William P. Robbins "Power Electronics: Converters, Applications, and Design," Wiley&Sons INC.
- [3] Editor in Chief Muhammad H. Rashid "Power Electronics Handbook" Academic Press
- [4] Nabae, A.; Takahashi, I.; Akagi, H., "A New Neutral-Point-Clamped PWM Inverter," IEEE Transactions on Industry Applications, vol. IA-17, no.5, pp.518,523, Sept. 1981
- [5] S. Buso, P. Mattarelli, "Digital Control in Power Electronics", Morgan&Claypool Publishers
- [6] K. Zhou, Kay-Soon Low, D. Wang, Fang-Lin Luo, B. Zhang, Y.Wang, "Zero-Phase Odd-Harmonic Repetitive Controller for a Single-Phase PWM Inverter", IEEE Transactions on Power Electronics, vol. 21, no. 1, Jan. 2006, pp.193-201.
- [7] R. Zhang, M. Cardinal, P. Szczesny, Dame, "A grid simulator with control of single-phase power converters in D-Q rotating frame," 33rd Annual IEEE Power Electronics Specialists Conference, 2002, vol.3, pp. 1431-1436.
- [8] B.A. Francis and W.M. Wonham, "The Internal Model Principle for Linear Multivariable Regulators", Appl. Math. Opt., 1975, pp.107-194.
- [9] R.W. Erickson, D. Maksimovic, "Fundamentals of Power Electronics", Second Edition, Springer-Verlag.
- [10] W. S. Levine, "The Control Handbook: Control System Fundamentals", Second Edition, CRC Press

- [11] R. Teodorescu, F. Blaabjerg, U. Borup, M. Liserre, “A New Control for Grid-Connected LCL PV Inverters with Zero Steady-State Error and Selective Harmonic Compensation”, Proc. of Applied Power Electronics Conference and Exposition, APEC 2004, vol. 1, pp. 580-586.
- [12] D. N. Zmood, D.G. Holmes, “Stationary frame current regulation of PWM inverters with zero steady-state error”, IEEE Transactions on Power Electronics, vol. 18, no. 3, May 2003, pp.814-822.
- [13] Y. Sato, T. Ishizuka, K. Nezu, T. Kataoka, “A New Control Strategy For Voltage-Type PWM Rectifiers To Realize Zero Steady-State Control Error in Input Current”, IEEE Transactions on Industry Applications, vol. 34, no. 3, May/June 1998, pp. 480-486.
- [14] N. Femia, G. Petrone, G. Spagnuolo, M. Vitelli, Power Electronics and Control Techniques for Maximum Energy Harvesting in Photovoltaic Systems, CRC press, 2012.
- [15] N. Femia, G. Petrone, G. Spagnuolo, M. Vitelli, “Optimization of Perturb and Observe Maximum Power Point Tracking Method”, IEEE Transactions on Power Electronics, vol. 20, no. 4, pp. 963-973, July 2005

Chapter 2

An improved Dead-Beat control based on an Observe&Perturb algorithm

For photovoltaic applications, high power three-phase inverters have been adopted due to the less number of devices and its lower cost. Moreover, there are very cheap computers able to manage complex tasks and, so, the solutions with the centralized inverters have become more attractive.

The multi-level topologies are usually the best choice to comply, more easily, with the regulation requirements in terms of current quality injected into the grid. Indeed, the dc input voltage is divided in several levels bringing the output voltage to have fewer harmonics and being more similar to a sinusoidal waveform. This kind of converters needs to have the voltage clamped in order to avoid the voltage unbalance between the different levels [1], [2].

The most important topologies are diode-clamped inverter, i.e. Neutral-Point Clamped (NPC), capacitor-clamped, i.e. Flying Capacitor (FC) and cascaded-inverters (CI) with separate dc source [3]. The first NPC inverter, a passive NPC [2], has unequal loss distribution among the semiconductor devices with the result that the temperature distribution of the semiconductor junction is asymmetrical. To solve this problem, an active NPC inverter has been developed [4]. A NPC-based inverter, the *AURORA ULTRA* of 1.4MW, is developed by *ABB Solar Group* mainly for the Asian market.

The design of a NPC inverter presents several issues. Besides the problems of efficiency optimization and of switches stress reduction, the system needs to be connected and synchronized to the grid. For poor quality grids, as the ones encountered in Asia, *ABB Solar Group* noticed that this time can be very long, also 33% of the total system development time. A time so long is necessary since the system must be adapted to the real grid conditions that can be totally different compared to the ideal ones. Great changes of frequency and root-means square value can happen and also the system must be able to

ensure the respect of the regulation requirements during the grid faults. Hence the setup of this inverter, mostly a fine tuning of the control parameters, is often done on the installation site because the grid has not only no ideal behavior but also local unpredictably characteristics that have to be take into account for the correct operation of the inverter.

Those considerations point out the need to explore new control techniques that allow having better performance both static and dynamic. The current control techniques, as described in the chapter 1, can be divided in two main categories: linear as the Proportional-Integral (PI) and the State Feedback Controller and non-linear as the hysteresis and the predictive with on line optimization [5].

A technique to be actually used by the industry must be well-known and reliable and, so, the most widely used is the PI technique also by *ABB Solar Group* for its converters. But in literature, there are a lot of works that analyzed different techniques like the Dead-Beat (DB) control and the sliding-mode (SM) control. The SM control has been implemented with stability proof and tested, where the SM control regulates the currents to suppress its harmonics getting a low THD and ensure desired amplitude and phase shift while keeping a good grid synchronization [6], [7]. The DB control is very attractive for its intrinsic excellent dynamic response [8-11] but a reliable and simple implementation has not been found yet. Hence, the focus of this chapter is a comparison between the widely used PI and the DB controls. Different implementation structures like dq and $\alpha\beta$ frames [12-14] can be used but as the focus is the two mentioned techniques the dq frame is selected. The modulation techniques for the NPC inverters are: multicarrier Pulse Width Modulation (PWM), Space Vector Modulation (SVM) and Selective Harmonic Elimination (SHE) [15], [16]. The multicarrier PWM is the most used for its simplicity of implementation. This technique can be divided in: Phase Disposition (PD), Phase Opposition Disposition (POD) and Alternative Phase Opposition Disposition (APOD) depending on how the carrier signals are taken [17], [18]. In this chapter, the PD PWM is selected because it has the lower THD [14] and the Neutral Point is balanced exploiting the modulation technique proprieties [19-22]. Hence, an improved DB control, based on a variation of the MPPT Perturb&Observe algorithm [23] described in the chapter 1 and for that called Observe& Perturb (O&P), is develop providing the general

guideline to select its parameters. Also a comprehensive comparison between the PI, the standard DB, a hybrid solution between the PI and DB called Integral+DB (I+DB) and the proposed O&P DB control is performed for passive NPC inverters with a dedicated simulation tool, written in C++ language, since the existing commercial software, such as Simulink[®], PSIM[®] and PSPICE[®], allow to make the analysis only a specific level: system, circuit or device. Both O&P method and simulation tool are not only for NPC inverters but they are very general being able to be applied to all the converters.

It worth be noted that for very high power systems, even if it is possible to emulate their dynamic in a scaled version system, the companies like *ABB Solar Group* usually prefer to test all the solutions in the final real system to be sure of the inverter behavior as the grid is already unpredictable. For this reason, in this chapter, the simulation results are presented and the proposed O&P DB control is implemented on a TMS320F28379D Dual-Core Delfino[™] Microcontroller (μc) to test the feasibility of all its components in a single embedded system. The choice of the F28379D μc is carried out to use the same family, the TI C2000, that *ABB Solar Group* implements on its converters and to have the best performance with a dual-core system.

2.1 Description of the simulator tool

The development of a simulation tool for a generic switching circuit has to take into account two aspects: to find the fundamental circuit equations and to detect the state of the switching devices.

In the implemented tool, exploiting the Chua-Lin algorithm [24], the normal tree and cotree are found and, then, the fundamental cutsets matrix is calculated in order to find the state model of the circuit. All the switches are model with a Piece-Wise Linear (PWL) Resistor with a great resistance value when the device is OFF and a very small resistance value when it is ON.

Hence, the software reads the topological information and the value of the single components by a text file and calculates the fundamental cutsets whose general expression is reported in the equations (2.1) and (2.2), where F_{xx} are the circuit topological

34 Chapter 2 An improved DB control based on an O&P algorithm
matrices and the symbols t and l denote that the component belongs to the tree and cotree respectively.

$$i = \begin{bmatrix} i'_E & i'_C & i'_R & i'_L & i'_R & i'_C \end{bmatrix}^T \quad v = \begin{bmatrix} v'_E & v'_C & v'_R & v'_L & v'_R & v'_C \end{bmatrix}^T \quad (2.1)$$

$$\begin{matrix} E^T & C^T & R^T & J^L & L^L & R^L & C^L \\ \left[\begin{array}{cccccccc} 1_E^T & 0 & 0 & 0 & F_{11} & F_{12} & F_{13} & F_{14} \\ 0 & 1_C^T & 0 & 0 & F_{21} & F_{22} & F_{23} & F_{24} \\ 0 & 0 & 1_R^T & 0 & F_{31} & F_{32} & F_{33} & F_{34} \\ 0 & 0 & 0 & 1_L^T & F_{41} & F_{42} & 0 & 0 \end{array} \right] & i = 0 & \end{matrix} \quad (2.2)$$

From the topological matrices, it is possible to find the circuit state model in a very simple way. Indeed, as shown by the equations (2.3)-(2.6), the state and the input matrices are calculated through only matrix operations.

$$\frac{dx(t)}{dt} = Ax(t) + Bu(t) \quad A = [M^{(0)}]^{-1} A^{(0)} \quad B = [M^{(0)}]^{-1} B^{(0)} \quad (2.3)$$

$$M^{(0)} = \begin{pmatrix} C_T + F_{24} C_L F'_{24} & 0 \\ 0 & L_{LL} - F'_{42} L_{TL} - L_{LT} F_{42} + F'_{42} L_{LL} F_{42} \end{pmatrix} \quad (2.4)$$

$$A^{(0)} = \begin{pmatrix} -F_{32} R^{-1} F'_{23} & -F_{22} + F_{23} R^{-1} F'_{33} R_T F_{32} \\ F'_{22} - F'_{32} G^{-1} F_{33} G_L F'_{23} & -F'_{32} G^{-1} F_{32} \end{pmatrix} \quad (2.5)$$

$$B^{(0)} = \begin{pmatrix} -F_{32} R^{-1} F'_{13} & -F_{21} + F_{23} R^{-1} F'_{33} R_T F_{31} \\ F'_{12} - F'_{32} G^{-1} F_{33} G_L F'_{13} & -F'_{32} G^{-1} F_{31} \end{pmatrix} \quad (2.6)$$

The state of the controlled switching devices (MOSFET, IGBT, etc.) is defined by the controller and by the modulator but it is necessary to detect the state of all synchronous devices (DIODE). These states are known for the specific application but, both to keep the software as more general as possible and both to analyze the circuit in any type of unpredictable conditions (grid and devices faults), the tool detects the synchronous switches state and checks the effective commutation of the controlled switches with an automatic and efficient method without a complete analysis of the circuit, exploiting the Compensation Theorem [25]. A commutation of the controlled devices imposed by the controller, with a PWL model, implies a change of resistance value in the switch branches and, so, a current variation in all branches of synchronous switches. If this variation is coherent with the previous state there is no commutation, otherwise there is and, hence, a new switch configuration can be analyzed in the same way. Thus, a consistent state of switching devices is found with a maximum of 3 steps, without calculating the state model for any configuration and then checking if it is coherent [25].

2.2 Standard controller design

The figure 2.1 shows the analyzed system. As can be seen, it is a three-level Neutral Point Diode Clamped Inverter described in the chapter 1. The PV source can be connected to the NPC input directly or, if it is necessary to adapt the PV voltage to the NPC input voltage, by means a further conversion stage. It worth be noted that, for grid connected inverters, the inductor L_g is usually not added as the grid impedance is present. The problem is that this impedance is unknown as it changes with the connection point to the grid. To take into account this case, the inductor L_g is not considered in the control techniques.

There are a lot of methodologies to control the output inverter phase currents I_a , I_b and I_c . The most intuitive is to use a controller for each phase current but it is possible to exploit the symmetrical proprieties of the three-phase systems in order to reduce the number of controllers from three to two as described in the chapter and so the control is performed exploiting the Park Transform in the dq frame.

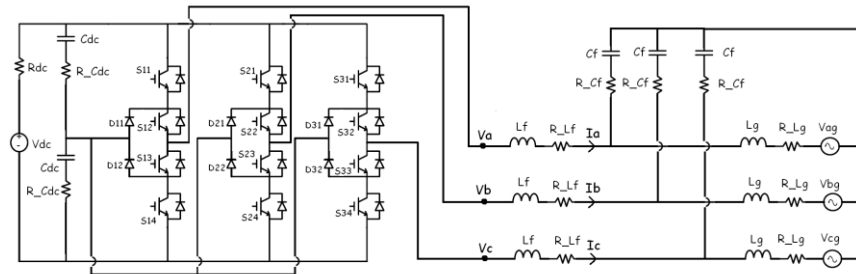


Fig 2.1 Neutral Point Clamped Inverter

The figure 2.2 shows the block diagram structure of this control.

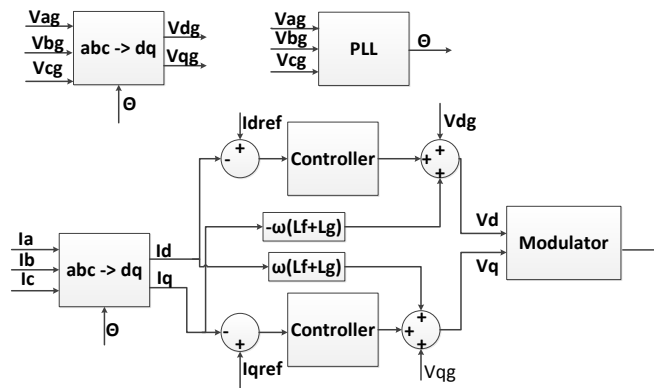


Fig 2.2 dq frame block diagram general structure

The Phase Disposition Carried-Based (PD-CB) PWM technique is adopted for this circuit since it has been demonstrated in literature that it leads to less harmonic distortion [14]. This technique is based on the comparison between the modulator signals, one for each inverter leg, and two triangular carried signals that are in phase. The modulation signals are achieved by an anti-transformation of the output control signals V_d and V_q in the abc frame. Also the neutral point (NP) balancing has been implemented through a DC link compensation added into the modulation as it is very similar to the balancing used by

37 Chapter 2 An improved DB control based on an O&P algorithm active NP voltage control techniques [20]. The figure 2.3 shows the block representation of the implemented modulation technique.

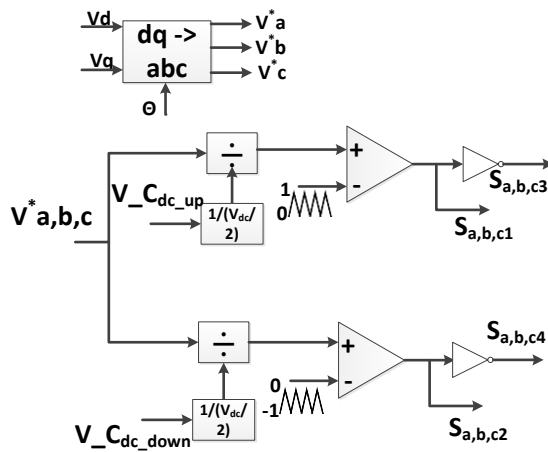


Fig 2.3 Phase Disposition Carried-Based Pulse Width Modulation

The circuit parameters, reported in the table 2.1, are based on the *AURORA ULTRA* inverter of *ABB Solar Group* and will be used for the controllers design and simulations of the next sections.

V_{dc}	700 V	R_{Lf}	1 m Ω
C_{dc}	1 mF	R_{cf}	1 m Ω
C_f	45 μ F	R_{Lg}	1 m Ω
L_f	250 μ H	R_{on_switch}	1 m Ω
L_g	45 μ H	R_{off_switch}	100 k Ω
R_{dc}	1 m Ω	$f_{switching}$	20 kHz
R_{cdc}	1 m Ω	f_{grid}	50 Hz
V_{g_rms}	186 V		

Table 2.1 Circuit Parameters

2.2.1 Proportional-Integral Linear Control design

The classical PI control loop with grid voltage feedforward is shown in the figure 2.4, where $G_{PI}(s)$ is the transfer function of the PI controller and $G_f(s)$ is the transfer function of the filter (the plant).

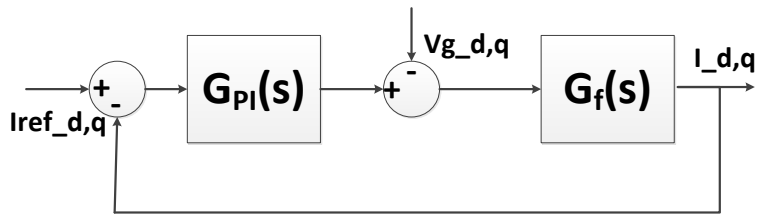


Fig. 2.4 PI current control loop

The effect of the capacitor C_f is neglected in the filter transfer function since the filter frequency response i/v with and without the capacitor is the same at the interest frequencies, as shown in the figure 2.5 with the values of the table 2.1. Hence, it is possible to define $L_T=L_g+L_f$ and $R_{LT}=R_{Lg}+R_{Lf}$.

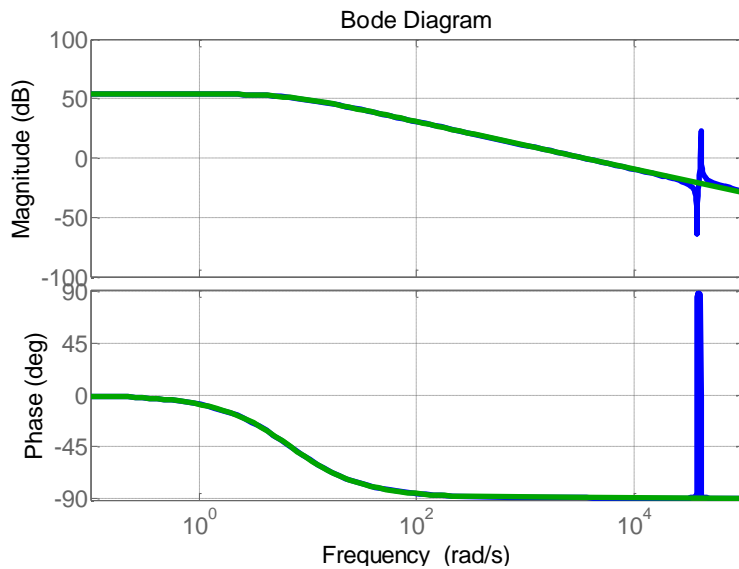


Fig 2.5 Filter frequency response i/v with (blue line) and without (green line) capacitor

The equations (2.7) and (2.8) show the transfer functions $G_{PI}(s)$ and $G_f(s)$.

$$G_f(s) = \frac{1}{R_T + sL_T} \quad (2.7)$$

$$G_{PI}(s) = k_p + \frac{k_I}{s} \quad (2.8)$$

To calculate k_p and k_I , a cross-over frequency f_c equal to 700Hz and a phase margin ϕ_m equal to 70° have been imposed to the open-loop gain transfer function $G_f(s)G_{PI}(s)$, with the values of the table 2.1, leading to the following values:

$$\begin{aligned} k_p &= 1.2 \\ k_I &= 2000 \text{ rad/s} \end{aligned} \quad (2.9)$$

Typically, a digital device, such as a microcontroller or a DSP, is used to implement this controller [26]. Hence, the transfer function $G_{PI}(s)$ is discretized with the Tustin transform as shown in the equations (2.10):

$$\begin{aligned} G_{PI}(s) &= k_p + \frac{k_I}{s} \xrightarrow{s = \frac{2}{Tc} \frac{z-1}{z+1}} G_{PI}(z) = k_p + k_I \frac{Tc}{2} \frac{z+1}{z-1} \rightarrow \\ &\rightarrow \begin{cases} u_I(kTc) = k_I Tc \frac{e(kTc) + e((k-1)Tc)}{2} + u_I((k-1)Tc) \\ V(kTc) = k_p e(kTc) + u_I(kTc) \end{cases} \end{aligned} \quad (2.10)$$

where $e(kTc) = i_{ref} - i(kTc)$ is the tracking error at the instant kTc .

The sampling frequency has been chosen to 20kHz, typical value used for this inverter by *ABB Solar Group*.

Also, coupled terms between the components d and q are also present with the Park Transform, as shown in the chapter 1, equation (1.5) and so decoupled compensation terms are added in the control laws [14], [26], as shown in the figure 2.2.

Thus, taking into account the feedforward grid voltage compensation and the decoupling term of the Park Transform, the following control laws are implemented:

$$\begin{cases} u_{dl}(kTc) = k_I Tc \frac{e_d(kTc) + e_d((k-1)Tc)}{2} + u_{dl}((k-1)Tc) \\ V_d(kTc) = k_P e_d(kTc) + u_{dl}(kTc) + V_{dg} - w L_T i_q(kTc) \end{cases} \quad (2.11)$$

$$\begin{cases} u_{ql}(kTc) = k_I Tc \frac{e_q(kTc) + e_q((k-1)Tc)}{2} + u_{ql}((k-1)Tc) \\ V_q(kTc) = k_P e_q(kTc) + u_{ql}(kTc) + V_{qg} + w L_T i_d(kTc) \end{cases}$$

2.2.2 Dead-Beat control design

The design of the DB control is carried out on the basis of the grid filter mathematical model [14], [26] in term of dq transformation where, as for the PI control, the capacitors C_f are neglected.

Looking at the figure 2.1 and defining $L_T = L_g + L_f$ and $R_{LT} = R_{Lg} + R_{Lf}$, it is possible to write [26]:

$$\frac{d}{dt} \begin{bmatrix} I_a \\ I_b \\ I_c \end{bmatrix} = \frac{R_{LT}}{L_T} \begin{bmatrix} 1 & 0 & 0 \\ 0 & 1 & 0 \\ 0 & 0 & 1 \end{bmatrix} \begin{bmatrix} I_a \\ I_b \\ I_c \end{bmatrix} + \frac{1}{3L_T} \begin{bmatrix} 2 & -1 & -1 \\ -1 & 2 & -1 \\ -1 & -1 & 2 \end{bmatrix} \begin{bmatrix} V_a \\ V_b \\ V_c \end{bmatrix} - \frac{1}{L_T} \begin{bmatrix} 1 & 0 & 0 \\ 0 & 1 & 0 \\ 0 & 0 & 1 \end{bmatrix} \begin{bmatrix} V_{ag} \\ V_{bg} \\ V_{cg} \end{bmatrix} \quad (2.12)$$

Considering the Park Transform of the system equations (2.12):

$$\frac{d}{dt} \begin{bmatrix} i_d \\ i_q \end{bmatrix} = \begin{bmatrix} -\frac{R_{LT}}{L_T} & w \\ -w & -\frac{R_{LT}}{L_T} \end{bmatrix} \begin{bmatrix} i_d \\ i_q \end{bmatrix} + \begin{bmatrix} \frac{1}{L_T} & 0 \\ 0 & \frac{1}{L_T} \end{bmatrix} \begin{bmatrix} V_d \\ V_q \end{bmatrix} + \begin{bmatrix} -\frac{1}{L_T} & 0 \\ 0 & -\frac{1}{L_T} \end{bmatrix} \begin{bmatrix} V_{gd} \\ V_{gq} \end{bmatrix} \quad (2.13)$$

41 Chapter 2 An improved DB control based on an O&P algorithm and applying to the (2.13) the Forward Euler method [26]:

$$\left. \frac{di}{dt} \right|_{t=kTc} = \frac{i((k+1)Tc) - i(kTc)}{Tc} \quad (2.14)$$

it is possible to calculate the discrete model at (k+1)-th instant:

$$\begin{bmatrix} i_d((k+1)Tc) \\ i_q((k+1)Tc) \end{bmatrix} = \begin{bmatrix} 1 - \frac{TcR_{LT}}{L_T} & Tc\omega \\ -Tc\omega & 1 - \frac{TcR_{LT}}{L_T} \end{bmatrix} \begin{bmatrix} i_d(kTc) \\ i_q(kTc) \end{bmatrix} + \begin{bmatrix} \frac{Tc}{L_T} & 0 \\ 0 & \frac{Tc}{L_T} \end{bmatrix} \begin{bmatrix} V_d(kTc) \\ V_q(kTc) \end{bmatrix} + \begin{bmatrix} -\frac{Tc}{L_T} & 0 \\ 0 & -\frac{Tc}{L_T} \end{bmatrix} \begin{bmatrix} V_{gd}(kTc) \\ V_{gq}(kTc) \end{bmatrix} \quad (2.15)$$

The sampling frequency is set equal to 20kHz as for the PI control. In principle, it is possible to set the currents i_d and i_q equal to the reference currents at the end of the sampling period, DB 1delay, neglecting the computation delay [26]:

$$\begin{aligned} i_d((k+1)Tc) &= i_{dref}(kTc) \\ i_q((k+1)Tc) &= i_{qref}(kTc) \end{aligned} \quad (2.16)$$

The equations (2.16) make the DB control very fast as it is able to lead i_d and i_q equal to the reference currents in 1 sampling time.

Replacing the (2.16) into the (2.15) and defining the errors $e_d(k) = i_{dref}(k) - i_d(k+1)$ and $e_q(k) = i_{qref}(k) - i_q(k+1)$, the control laws are determined:

$$\begin{aligned} V_d(kTc) &= \frac{L_T}{Tc} e_d(Tck) + R_{LT} i_d(kTc) - L_T \omega i_q(kTc) + V_{gd}(kTc) \\ V_q(kTc) &= \frac{L_T}{Tc} e_q(Tck) + R_{LT} i_q(kTc) - L_T \omega i_d(kTc) + V_{gq}(kTc) \end{aligned} \quad (2.17)$$

As a real digital device needs a finite time to perform the calculations, the currents i_d and i_q have to be set equal to the reference currents at the end of next sampling time, DB 2delay:

$$\begin{aligned} i_d((k+2)Tc) &= i_{dref}(kTc) \\ i_q((k+2)Tc) &= i_{qref}(kTc) \end{aligned} \quad (2.18)$$

but the DB control keeps very fast as $T_c \ll T_{grid}$.

Writing the discrete model from the (2.13) for the $(k+2)$ -th instant with the Forward Euler method, replacing the (2.15) in the result and neglecting the parasitic resistances R_T as it is usually done [26], the control laws, shown in the equations (2.19), can be written:

$$\begin{aligned} V_d((k+1)Tc) &= \frac{L_T}{Tc} e_d(Tck) - V_d(kTc) + V_{gd}(kTc) + V_{gd}((k+1)Tc) - L_T w [i_q(kTc) + i_q((k+1)Tc)] \\ V_q((k+1)Tc) &= \frac{L_T}{Tc} e_q(Tck) - V_q(kTc) + V_{gq}(kTc) + V_{gq}((k+1)Tc) + L_T w [i_d(kTc) + i_d((k+1)Tc)] \end{aligned} \quad (2.19)$$

Since the sampling frequency is much greater than the grid frequency ($f_c=20\text{kHz} \gg f_{grid}=50\text{Hz}$), it is possible to set:

$$\begin{aligned} V_{gd}((k+1)Tc) &\approx V_{gd}(kTc) \\ i_q((k+1)Tc) &\approx i_q(kTc) \\ V_{gq}((k+1)Tc) &\approx V_{gq}(kTc) \\ i_d((k+1)Tc) &\approx i_d(kTc) \end{aligned} \quad (2.20)$$

Thus, replacing the (2.20) into the (2.19), the final control laws are calculated:

$$\begin{aligned} V_d((k+1)Tc) &= \frac{L_T}{Tc} e_d(kTc) - V_d(kTc) + 2V_{gd}(kTc) - 2L_T w i_q(kTc) \\ V_q((k+1)Tc) &= \frac{L_T}{Tc} e_q(kTc) - V_q(kTc) + 2V_{gq}(kTc) + 2L_T w i_d(kTc) \end{aligned} \quad (2.21)$$

It worth be noted that as all the control laws (2.17), (2.19) and (2.21) are strongly dependent by the model assumptions, the DB control is not able to guarantee zero tracking errors.

The Dead-Beat stability analysis [14], [26] can be done starting from the (2.15) that can be written as:

$$\begin{aligned} i_d((k+1)Tc) &= ai_d(kTc) + b(V_d(kTc) - V_{gd}(kTc)) + ci_q(kTc) \\ i_q((k+1)Tc) &= ai_q(kTc) + b(V_q(kTc) - V_{gq}(kTc)) - ci_d(kTc) \end{aligned} \quad (2.22)$$

where

$$a = 1 - \frac{TcR_{LT}}{L_T}$$

$$b = \frac{Tc}{L_T}$$

$$c = Tcw$$

Looking at the (2.22), it is possible to note the cross-coupling term $\pm c$ due to the Park Transform as described in the chapter 1, equation (1.5). As shown in the figure 2.2, like for the PI control, decoupled compensation terms [14], [26] have been introduced that are the terms $\pm L_T\omega$ in the (2.17) and $\pm 2L_T\omega$ in the (2.21) making the (2.22) decoupled equations. Hence, it is possible to write:

$$i_d((k+1)Tc) = ai_d(kTc) + b(V_d(kTc) - V_{gd}(kTc)) \quad (2.23)$$

Where only the d component is considered as the same results can be found for the q component.

Applying the Z-transform to the equation (2.23):

$$zI_d(z) = aI_d(z) + bU(z) \quad (2.24)$$

where

$$u(k) = V_d(kTc) - V_{gd}(kTc)$$

the plant transfer function is:

$$G_f(z) = \frac{I_d(z)}{U(z)} = \frac{bz^{-1}}{1-az^{-1}} \quad (2.25)$$

That is stable having 1 pole in $a=(1-T_c R_{LT}/L_T)<1$.

In the design of the DB control, it has been set that the current is equal to the reference current at the end of 1 or 2 sampling periods, as shown in the equations (2.16) and (2.18). Hence the closed-loop transfer function can be found applying the Z-Transform to the (2.18):

$$G_{CL}(z) = \frac{1}{z^2} \quad (2.26)$$

with $k=1$ or 2 and the DB transfer function becomes:

$$G_{DB}(z) = \frac{1}{G_f(z)} \frac{z^{-2}}{1-z^{-2}} = \frac{1}{b} \frac{1-az^{-1}}{z-z^{-1}} \quad (2.27)$$

The equation (2.26) has 2 poles in the origin and so the closed-loop system is stable.

As for the tracking errors d and q , also the stability is affected by the model mismatch but the robustness of the DB control is very high [9], [26]. Considering a mismatch of the inductor $L_T = L_T \pm \Delta L_T$, i.e. replacing this value only in the (2.25) and calculating the poles using also the (2.27), the poles of the closed loop systems are [9]:

$$p_{1,2} = \pm \sqrt{\frac{\Delta L_T}{L_T}} \quad (2.28)$$

The equation (2.28) shows that unless there is a model mismatch of 100% L_T , the system remains stable.

Hence, the model mismatch affects principally the state-state errors d and q .

2.2.3 Hybrid solution: Dead-Beat and integral action

As described in the previous section, the DB control has a very fast dynamic but presents a steady-state tracking error of a no zero value. A first way to try to achieve that keeping the advantage of a fast dynamic is a hybrid solution with an integral action that guarantee the zero tracking error in steady-state condition: an Integral+DB (I+DB) control. The integral action does not have to affect the dynamic of the DB, i.e. ki values more and more close to the (2.9) lead to system dynamic more and more similar to the PI dynamic, not justifying the use of the DB control anymore. But, decreasing ki , the integral action is not able to lead the average tracking error rapidly to zero. Considering a trade-off between these two requirements, ki has been set to 1/20 of the (2.9) and so $ki=2000/20\text{rad/s}=100\text{rad/s}$. This is the limit of this solution: the average tracking error can be lower than the DB but not yet zero as for the PI control because to keep the fast dynamic of the DB, the integral action should be very slow, as it will be shown with the simulation results.

2.3 Observe&Perturb Dead-Beat control

The proposed method is based on the MPPT Perturb&Observe algorithm [24]. Since this algorithm first observes and then makes a perturbation is called Observe&Perturb (O&P).

The goal of this control is to achieve a zero tracking error in steady-state condition without affecting the dynamic response of the standard DB control described in the previous section.

As the P&O [24], perturbations, ΔV_d and ΔV_q , are introduced by the controller at fixed time step T_a in the control laws (2.17) and (2.21) determining the equations (2.28), O&P DB 1delay, and (2.29), O&P DB 2delay:

$$\begin{aligned} V_d((n+1)Ta) &= \frac{L_r}{T_c} e_d(nTa) + R_{LT} i_d(nTa) - L_r \omega i_q(nTa) + V_{gd}(nTa) + \Delta V_d \\ V_q((n+1)Ta) &= \frac{L_r}{T_c} e_q(nTa) + R_{LT} i_q(nTa) - L_r \omega i_d(nTa) + V_{gq}(nTa) + \Delta V_q \end{aligned} \quad (2.28)$$

$$\begin{aligned}
V_d((n+1)Ta) &= \frac{L_T}{T_c} e_d(nTa) - V_d(nTa) + 2V_{gd}(nTa) - 2L_T w_i q(nTa) + \Delta V t_d \\
V_q((n+1)Ta) &= \frac{L_T}{T_c} e_q(nTa) - V_q(nTa) + 2V_{gq}(nTa) + 2L_T w_i d(nTa) + \Delta V t_q
\end{aligned}
\tag{2.29}$$

Hence the controller, for $k \neq nTa$ uses the (2.17) and (2.21) and for $k = nTa$, the (2.28) and (2.29). It worth be noted that the DB 1delay, equations (2.17) and (2.28), is considered as theoretical case study.

As in the [27] Ta was related to the settling time of the step response, Ta for the O&P is set in order to do not affect the stability of the system, i.e. the system needs to reach the next steady state point before to have a new perturbation. In this way, these perturbations do not have to be considered in the loop as they are an optimization of the operating point, as for the P&O [23].

For the DB control, looking at the equations (2.16) and (2.18), the new steady state is reached after 1 or 2 sampling periods [14] and so:

$$Ta > 2Tc \tag{2.30}$$

indicating with Tc the sampling period. To have some margin on this condition, Ta has been chosen equal to $5(2Tc) = 500\mu s$.

The perturbations, ΔV_d and ΔV_q , are calculated on the basis of the average errors of the component d and q that is runtime calculated at the fixed time Ta :

$$E_{d_mean} = \frac{\sum_{k=1}^N e_d(k)}{N} \tag{2.31}$$

$$E_{q_mean} = \frac{\sum_{k=1}^N e_q(k)}{N} \tag{2.32}$$

where $N = Ta/Tc = 10$.

The bigger the average errors, the bigger has to be the perturbations magnitude while the perturbations sign is the same of the average error sign. Hence ΔV_d and ΔV_q are increased or decreased of values $\Delta\Delta V_d$ and $\Delta\Delta V_q$ that are much bigger when the relative average error absolute value increases. The figure 2.6 shows the flowchart of the algorithm that highlights the low computational effort of this technique since there are no complex operations but only two average value calculations, a series of seven "if" conditions and 1 addition.

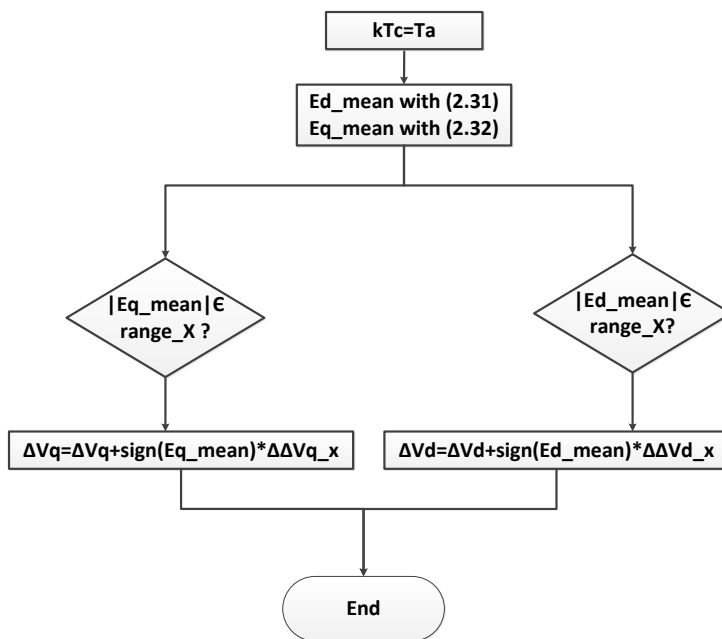


Fig 2.6 O&P algorithm flowchart

Taking into account the maximum reference currents, I_{dref_max} and I_{qref_max} to set and noticing that the aim is to achieve a zero error, the perturbations have to be more granular around zero and, so, a look-up table can be defined with 7 thresholds for the average errors and, consequently, 7 perturbation magnitudes $\Delta\Delta V_d$ and $\Delta\Delta V_q$.

The values for the average errors can be determined setting a minimum and maximum percent errors, $(E_{d,q_mean}/I_{d,qref_max} * 100)$, that are desired while for $\Delta\Delta V_d$ and $\Delta\Delta V_q$ the minimum and maximum variation of V_d and V_q that corresponds to a minimum and maximum variation of the voltages V_a , V_b and V_c of the figure 2.1. Also the maximum perturbation amplitudes, ΔV_{dmax} and ΔV_{qmax} have to be much smaller of the V_{dmax} and V_{qmax} in order to do not affect the dynamic and the stability of the system in the (2.28) and (2.29) [24].

For the application considered in this chapter, based on the parameters of the table 2.1, I_{dref_max} is 392A and I_{qref_max} is 675A. Setting $\Delta V_{dmax} = \Delta V_{qmax} < 6\% V_{dqmax} = 20V$, it is possible to find the values, shown in the table 2.2 for the (2.28) and in the table 2.3 for the (2.29), where the percent errors are set from 0.025% to 25.5% and the $\Delta\Delta V_{d,q}$ from 6% to 0.05% with $V_{dqmax} < 6\% V_{dc}/2 = 20V$. The fine tuning of these values has been performed through simulations to get the best result in terms of tracking errors and dynamic.

Range_x (%Ed,q_mean)	$\Delta\Delta V_d$ (%Vd)	$\Delta\Delta V_q$ (%Vq)
$0.025 < E_{d,q_mean} < 0.125$	0.057	0.085
$0.125 < E_{d,q_mean} < 0.25$	0.11	0.2
$0.25 < E_{d,q_mean} < 2.5$	0.22	0.42
$2.5 < E_{d,q_mean} < 7.65$	0.57	0.57
$7.65 < E_{d,q_mean} < 12.75$	1.42	1.42
$12.75 < E_{d,q_mean} < 25.5$	2.85	2.85
$ E_{d,q_mean} > 25.5$	5.71	5.71

Table 2.2 Perturbation Magnitude for the (2.28)

Range_x (%E _{d,q_mean})	$\Delta\Delta V_d$ (%Vd)	$\Delta\Delta V_q$ (%Vq)
$0.025 < E_{d,q_mean} < 0.125$	0.14	0.28
$0.125 < E_{d,q_mean} < 0.25$	0.28	0.42
$0.25 < E_{d,q_mean} < 2.5$	0.42	0.57
$2.5 < E_{d,q_mean} < 7.65$	0.85	0.85
$7.65 < E_{d,q_mean} < 12.75$	1.42	1.42
$12.75 < E_{d,q_mean} < 25.5$	2.85	2.85
$ E_{d,q_mean} > 25.5$	5.71	5.71

Table 2.3 Perturbation Magnitude for the (2.29)

2.4 Simulation results

In this section, the simulation results are reported for the previously designed controllers, O&P DB, I+DB and PI with the circuit parameters of the table 2.1. The same conditions and assumptions are considered as in this way the different results are caused only by the different control techniques.

In the figure 2.7, the grid phase voltages imposed to the circuit are shown. They are a balanced and symmetrical three-phase sinusoidal voltage system with no added noise. The frequency is 50Hz while the rms value is 186V in normal grid condition. A symmetrical grid fault occurs at 0.1s and persists for 145ms with a change in the rms value from 186V to 2.96V.

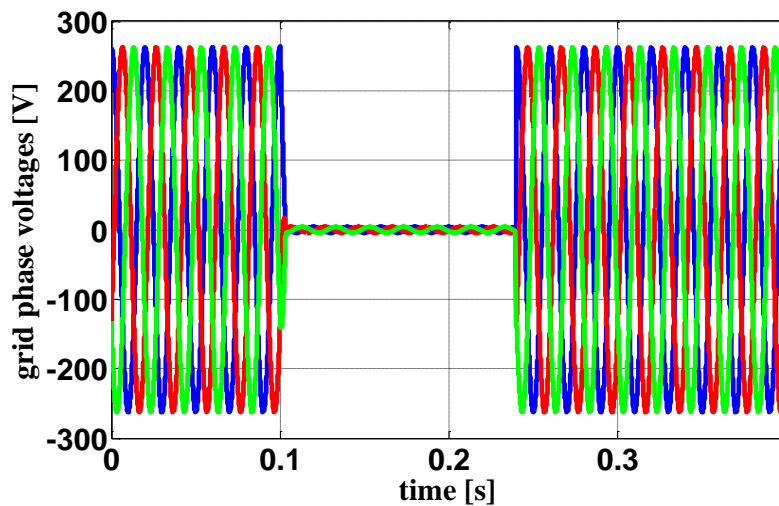


Fig 2.7 Grid phase voltages

The reference currents profiles are depicted in the figure 2.8. In normal grid condition, the d current component has to be equal to 392A while the q current component has to be equal to 0 to inject only active power into the grid. During the grid fault, after a transition time where the current components are set to zero, the regulation requirements impose that the system injects into the grid also a big reactive power that means high q component. For this simulation, a value of 675A for the q component and 80A for the d component is set after a liner increment from zero.

50 Chapter 2 An improved DB control based on an O&P algorithm
 All this data has been provided by *ABB Solar Group* and is referred to a real case in the Indian grid.

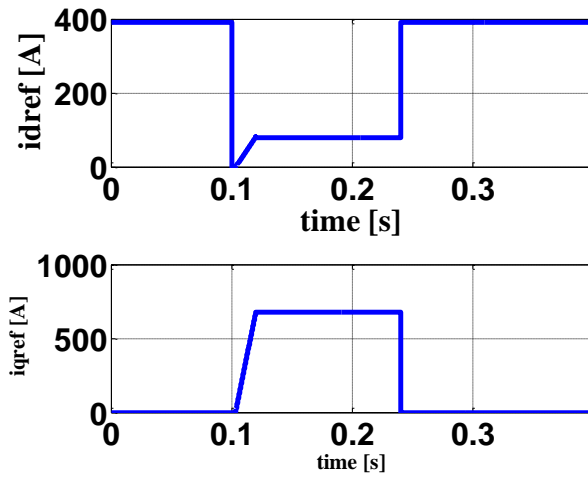


Fig 2.8 Reference currents

The figures 2.9 and 2.10 show the simulation results for the d component while the figure 2.11 and 2.12 for the q component in term of the tracking error. The aim of these figures is to analyze 2 characteristic of the waveforms: the capability to go to zero and their speed to achieve that.

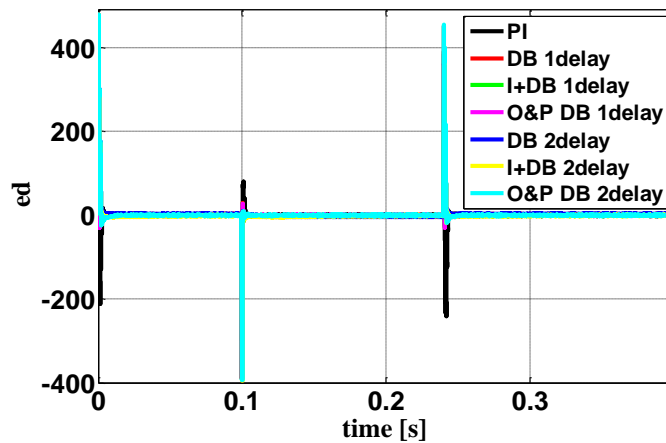


Fig 2.9 d component tracking errors

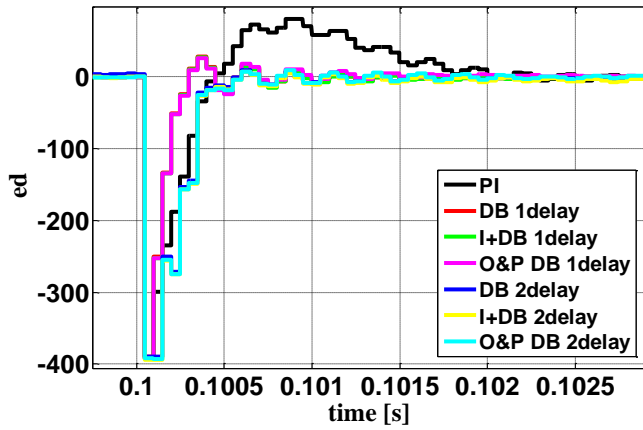


Fig 2.10 Zoom of d component tracking errors when the reference changes

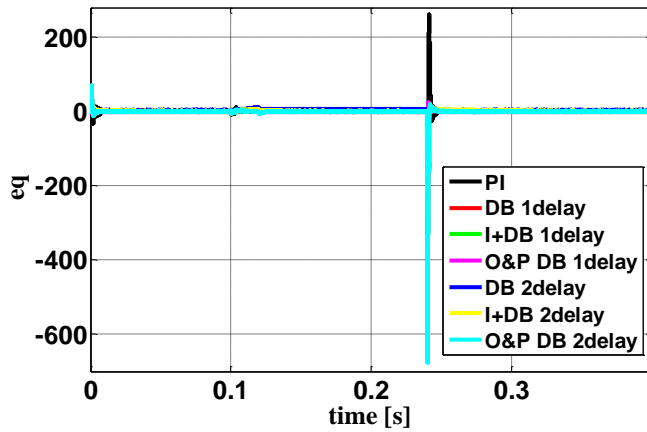


Fig 2.11 q component tracking errors

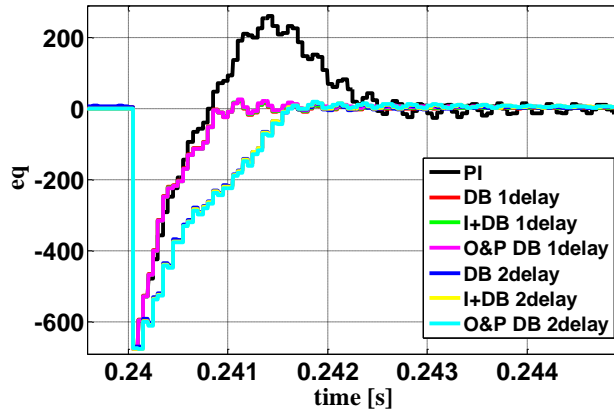


Fig 2.12 Zoom of q component tracking errors when the reference changes

As the dynamic is related to the kind of implemented controller, it is possible to identify the PI dynamic, the DB 1delay dynamic and the DB 2delay dynamic while the I+DB and O&P DB dynamics are very similar to the standard DB dynamic.

In the table 2.4, the results for the d component are reported.

	PI	DB_1d	DB_2d	DB+I_1d	DB+I_2d	DB +O&P_1d	DB +O&P_2d
%ed_average	0	0.44	0.89	0.08	0.17	0	0
Settling time at the start-up	2.5ms	0.9ms	1.9ms	1ms	1.9ms	0.9ms	1.9ms
Settling time at the grid fault	2ms	0.3ms	0.6ms	0.6ms	0.6ms	0.3ms	0.6ms
Settling time after the grid fault	3.2ms	1ms	2ms	1.2ms	2ms	1ms	2ms

Table 2.4 d components results

Considering the d average error equal to zero for a value less than 0.001%, it is possible to see that only the PI and the O&P are able to reach a zero error. The other techniques present a finite error even if limited. Also, the O&P DB has the same dynamic of the standard DB that is faster than the PI dynamic. It worth be noted that having implemented exactly the equations (2.17) and (2.21), the error of the

53 Chapter 2 An improved DB control based on an O&P algorithm
 DB and DB+I is not related to a model mismatch but is intrinsic in the Dead-Beat technique.

The table 2.5 shows the results for the q component where it is not reported the percent error because $I_{qref}=0$ but the absolute average error.

	PI	DB_1d	DB_2d	DB+I_1d	DB+I_2d	DB +O&P_1d	DB +O&P_2d
eq_average	0.01A	1.54A	3.07A	0.71A	1.41A	0.01A	0.0043A
Settling time at the start-up	8ms	0.9ms	2ms	1ms	2ms	1ms	1.5ms
Settling time after the grid fault	2.5ms	1ms	1.6ms	1ms	1.6ms	1ms	1.6ms

Table 2.5 q components results

The same consideration and conclusions of the d component are possible for the q component: the O&P technique is able to reach the same steady-state performance of the PI keeping the fast dynamic of the DB while the other techniques having a fast dynamic are not able to lead the error to zero.

It is clear that the DB control, starting from the values of the table 2.4 and 2.5, has greater errors when there is a model mismatch, i.e. when the equations (2.17) and (2.18), from which the equations of the O&P and I+DB are obtained, are not equal to the model of the plant. Hence, a simulation has been performed when there is no feed-forward compensation, i.e. V_{gd} and V_{gq} are not considered. The results of this simulation for the d component are depicted in the figures 2.13-2.15, as the same consideration can be done for the q component.

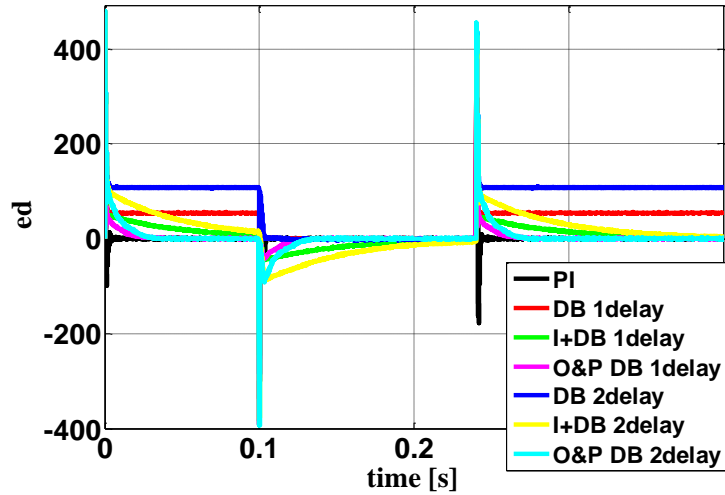


Fig 2.13 d component tracking errors with no grid voltage compensation

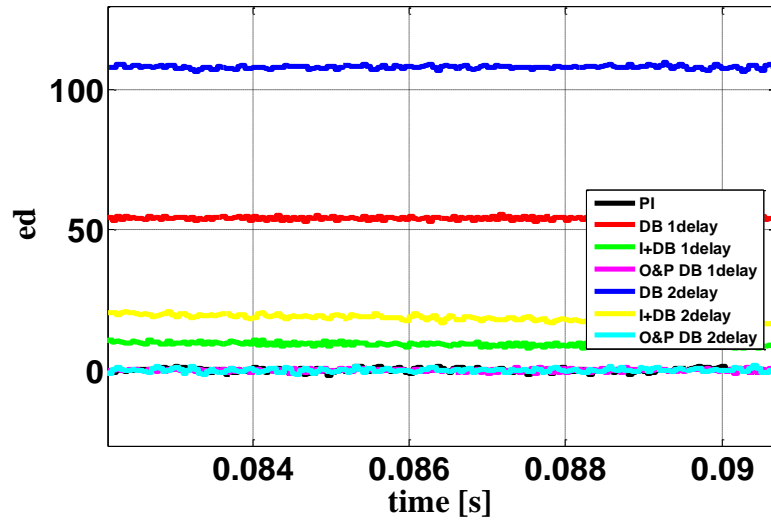


Fig 2.14 Zoom of the d component tracking errors with no grid voltage compensation at steady-state condition

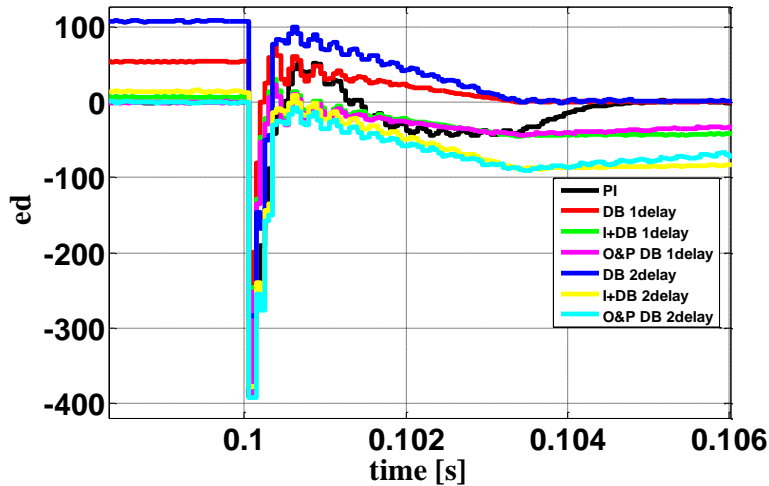


Fig 2.15 Zoom of d component tracking errors with no grid voltage compensation when the reference changes

These figures highlight that the PI control is able to lead the error to zero due to the integral action while the DB control presents a fixed, not eliminable error, around 14% for the DB 1delay and around 28% for the DB 2 delay. The I+DB is better than the DB but it has a very slow dynamic having a result a no zero error, figure 2.13. As shown in the figure 2.14, the O&P DB is able to lead the error to zero even in this extreme condition but the PI control is faster. The aim of this simulation has been to demonstrate that in any kind of condition, with the O&P method zero tracking errors can be obtained but it is clear that the speed convergence to zero depends by how big is this error. It worth be noted that a value for the grid feedforward is usually present in the model, like the grid reference value, and in this condition the impact on the system is reduced and the dynamic of the O&P become faster.

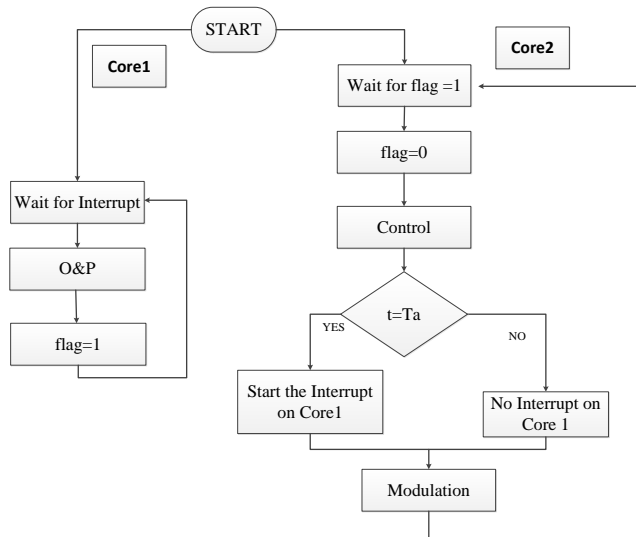
2.5 Implementation on a microcontroller

The O&P DB control has been implemented on the F28379D Delfino™ Experimenter Kit shown in the figure 2.16 to test the feasibility of all its components, i.e. O&P algorithm, control and modulation, on a single embedded system.



Fig 2.16 F28379D Delfino™ Experimenter Kit

The TMS320F28379D is a 32-bit dual core microcontroller (μc) with the 2 identical cores in terms of memory resources, peripherals and computational performance. To maximize the use of the dual core system, the first core has been used to perform the O&P algorithm and the second core to implement the control and the modulation. Looking at the figures 2.2 and 2.3, the controller and modulator inputs are the 3 grid currents, the 3 grid voltages and the 2 clamped capacitor voltages that, for this implementation, have been taken from the simulation results of the previous section. Based on the memory of F28379D and the sampling frequency of 20kHz, 50 samples per input have been stored that means a simulation time of 2.5ms. The figure 2.17 shows the flowchart of the program that has been implemented through an interrupts system and a shared memory.

Fig 2.17 μ c program flowchart

Hence, the program performs the following actions at each time instant based on the figure 2.2 and 2.3, after the initialization and the start of the program on the Core2:

- wait for flag=1 to make sure that the Core1 has finished to perform the O&P algorithm
- control: Park Transform of the grid currents and voltages and V_d and V_q calculation with the (2.21)
- if $t=Ta$, time step of the O&P algorithm, start the interrupt on the Core1
- modulation: V_a^* , V_b^* , V_c^* calculation, with the Park anti-transform of V_d and V_q and 12 gate signals calculation S_{xx} comparing V_a^* , V_b^* and V_c^* with 2 emulated triangular waveforms.

While the below actions are performed in the Core1 interrupt for the O&P every T_a , looking at the figure 2.6:

- E_d_mean and E_q_mean calculation
- based on the tables 2.2 and 2.3, $\Delta\Delta V_d$ and $\Delta\Delta V_q$ calculation

It worth be noted that this implementation is ready to be tested on a real system replacing the stored inputs with the inverter quantities acquired by the μc through sensors and analog to digital converters and sending the S_{xx} signal to the gate drivers of the inverts through the GPIO pins of the μc .

The debug and expression windows of the Code Composer Studio, the integrated development environment (IDE) tools for this μc , are shown in the figures 2.18 and 2.19 to highlight that the 2 cores are working and performing the calculation.

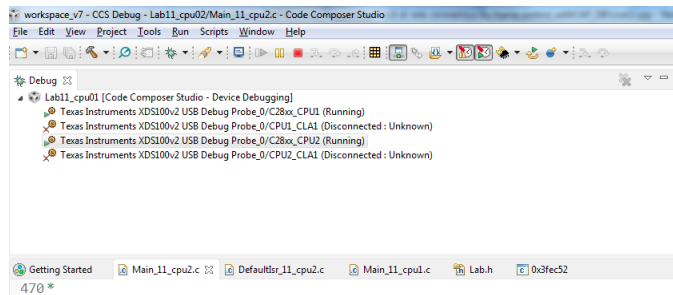


Fig 2.18 Code Composer debug window

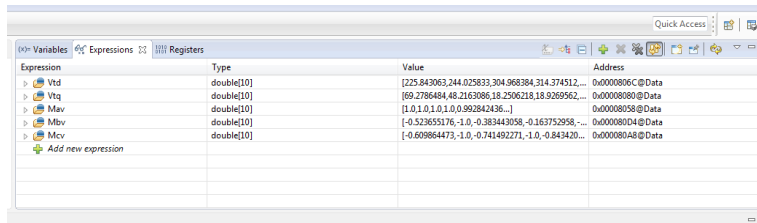


Fig 2.19 Code Composer Studio variables window

The results of this implementation are shown in tables 2.6-2.8 with 10 grid currents samples, 10 modulation signals from the tool simulation and 10 from the μc .

t (s)	I _a (A)	I _b (A)	I _c (A)
0.000249	-34.4039	9.221822	25.18209
0.000499	48.59125	-42.8085	-5.78275
0.000749	134.2136	-91.8734	-42.3401
0.000999	189.0857	-81.5942	-107.492
0.001249	223.9116	-44.3782	-179.533
0.001499	266.2396	-20.8466	-245.393
0.001749	301.4603	12.04249	-313.503
0.001999	310.0451	46.72021	-356.765
0.002249	295.1438	76.71205	-371.856
0.002499	277.5713	106.676	-384.247

Table 2.6 Grid currents

t (s)	V _a *	V _b *	V _c *
0.000249	1	-0.52366	-0.60986
0.000499	1	-1	-1
0.000749	1	-0.38344	-0.74149
0.000999	1	-0.16375	-1
0.001249	0.992843	-0.14942	-0.84342
0.001499	1	0.061955	-1
0.001749	0.83413	0.064901	-0.89903
0.001999	0.744905	0.139671	-0.88458
0.002249	0.648082	0.216584	-0.86467
0.002499	0.56788	0.27882	-0.8467

Table 2.7 Modulating signals from the tool simulation

t (s)	V _a *	V _b *	V _c *
0.000249	1	-0.52366	-0.60986
0.000499	1	-1	-1
0.000749	1	-0.38344	-0.74149
0.000999	1	-0.16375	-1
0.001249	0.992842	-0.14942	-0.84342
0.001499	1	0.061956	-1
0.001749	0.83413	0.0649	-0.89903
0.001999	0.744904	0.139672	-0.88458
0.002249	0.648082	0.216584	-0.86467
0.002499	0.567879	0.278822	-0.8467

Table 2.8 Modulating signals from the μ c

Comparing the tables 2.7 and 2.8, it is possible to note that the 2 simulations lead to the same results demonstrating the feasibility of the O&P DB control with all its components, i.e. O&P algorithm, control and modulation, on a single embedded system making it suitable for digital systems.

References

- [1] Yazdani A., Iravani R., "Voltage-Sourced Converters in Power Systems – Modeling, Control and Applications", IEEE Press, WILEY
- [2] Nabae, A.; Takahashi, I.; Akagi, H., "A New Neutral-Point-Clamped PWM Inverter," IEEE Transactions on Industry Applications, vol. IA-17, no.5, pp.518,523, Sept. 1981
- [3] Rodriguez, J.; Jih-Sheng Lai; Fang Zheng Peng, "Multilevel inverters: a survey of topologies, controls, and applications," IEEE Transactions on Industrial Electronics, vol.49, no.4, pp.724,738, Aug 2002
- [4] Rodriguez, J.; Bernet, S.; Steimer, P.K.; Lizama, I.E., "A Survey on Neutral-Point-Clamped Inverters," IEEE Transactions on Industrial Electronics, vol.57, no.7, pp.2219,2230, July 2010.
- [5] Kazmierkowski, M.P.; Malesani, L., "Current control techniques for three-phase voltage-source PWM converters: a survey," IEEE Transactions on Industrial Electronics, vol.45, no.5, pp.691,703, Oct 1998
- [6] F. Sebaaly, H. Vahedi, H. Y. Kanaan, N. Moubayed, K. Al-Haddad, "Design and Implementation of Space Vector Modulation-Based Sliding Mode Control for Grid-Connected 3L-NPC Inverter," IEEE Transactions on Industrial Electronics, vol. 63, no. 12, pp. 7854-7863, Dec. 2016.
- [7] A. Bouzidi, M. L. Bendaas, S. Barkat, M. Bouzidi, "Sliding mode control of three-level NPC inverter based grid-connected photovoltaic system," 2017 6th International Conference on Systems and Control (ICSC), Batna, 2017, pp. 354-359.
- [8] Malesani, L.; Mattavelli, P.; Buso, S., "Robust dead-beat current control for PWM rectifiers and active filters," IEEE Transactions on Industry Applications, vol.35, no.3, pp.613,620, May/Jun 1999

- [9] Rodriguez, J.; Pontt, J.; Silva, C.A.; Correa, P.; Lezana, P.; Cortes, P.; Ammann, U., "Predictive Current Control of a Voltage Source Inverter," IEEE Transactions on Industrial Electronics, vol.54, no.1, pp.495,503, Feb. 2007
- [10] Vargas, R.; Cortes, P.; Ammann, U.; Rodriguez, J.; Pontt, J., "Predictive Control of a Three-Phase Neutral-Point-Clamped Inverter," IEEE Transactions on Industrial Electronics, vol.54, no.5, pp.2697,2705, Oct. 2007
- [11] Rodriguez, J.; Pontt, J.; Cortes, P.; Vargas, R., "Predictive Control of a Three-Phase Neutral Point Clamped Inverter," IEEE 36th Power Electronics Specialists Conference, 2005. PESC '05., pp.1364,1369, 16-16 June 2005
- [12] Blaabjerg, F.; Teodorescu, R.; Liserre, M.; Timbus, A.V., "Overview of Control and Grid Synchronization for Distributed Power Generation Systems," IEEE Transactions on Industrial Electronics, vol.53, no.5, pp.1398, 1409, Oct. 2006
- [13] Timbus, A.; Liserre, M.; Teodorescu, R.; Rodriguez, P.; Blaabjerg, F., "Evaluation of Current Controllers for Distributed Power Generation Systems," IEEE Transactions on Power Electronics, vol.24, no.3, pp.654,664, March 2009
- [14] Teodorescu R., Liserre M., Rodriguez P., "Grid Converters for Photovoltaic and Wind Power System", IEEE Press, WILEY
- [15] Holtz, J., "Pulsewidth modulation-a survey," IEEE Transactions on Industrial Electronics, vol.39, no.5, pp.410,420, Oct 1992
- [16] Holmes D., Lipo T., "Pulse Width Modulation For Power Converters - Principles and Practice", IEEE Press, WILEY-INTERSCIENCE
- [17] Kouro, S.; Lezana, P.; Angulo, Mauricio; Rodriguez, J., "Multicarrier PWM With DC-Link Ripple Feedforward Compensation for Multilevel Inverters," IEEE Transactions on Power Electronics, vol.23, no.1, pp.52,59, Jan. 2008

- [18] McGrath, B.P.; Holmes, D.G., "Multicarrier PWM strategies for multilevel inverters," IEEE Transactions on Industrial Electronics, vol.49, no.4, pp.858, 867, Aug 2002
- [19] Mohzani, Z.; McGrath, B.P.; Holmes, D.G., "The balancing properties of DC link compensation for 3-phase Neutral Point Clamped (NPC) Converter," 2012 7th International Power Electronics and Motion Control Conference (IPEMC), vol.1, pp.574,579, 2-5 June 2012
- [20] du Toit Mouton, H., "Natural balancing of three-level neutral-point-clamped PWM inverters," IEEE Transactions on Industrial Electronics, vol.49, no.5, pp.1017,1025, Oct 2002
- [21] Celanovic, N.; Boroyevich, D., "A comprehensive study of neutral-point voltage balancing problem in three-level neutral-point-clamped voltage source PWM inverters," IEEE Transactions on Power Electronics, vol.15, no.2, pp.242,249, Mar 2000
- [22] Holmes, Lipo, "Pulse Width Modulation for Power Converters - Principles and Practice", IEEE Press.
- [23] N. Femia, G. Petrone, G. Spagnuolo, M. Vitelli, Power Electronics and Control Techniques for Maximum Energy Harvesting in Photovoltaic Systems, CRC press, 2012.
- [24] Chua-Lin, "Computer-Aided Analysis of Electronic Circuits – Algorithms and Computational Techniques", Englewood Cliffs, NJ: Prentice-Hall.
- [25] N.Femia, "Understanding commutations in switching converters. I. Basic theory and application of the Compensation Theorem, "Transactions on Aerospace and Electronic Systems, IEEE vol.39, no.1, pp.282, 297, Jan. 2003.
- [26] S. Buso, P. Mattarelli, "Digital Control in Power Electronics", Morgan&Claypool Publishers

64 Chapter 2 An improved DB control based on an O&P algorithm
[27] N. Femia, G. Petrone, G. Spagnuolo, M. Vitelli, "Optimization of
Perturb and Observe Maximum Power Point Tracking Method",
IEEE Transactions on Power Electronics, vol. 20, no. 4, pp. 963-
973, July 2005

Chapter 3

The Effect of a Constant Power Load on the Stability of a Smart Transformer

The high penetration of renewable energy source has led great changes in the electric grid. The conventional grid was composed of a source, a distribution energy system and loads. Instead, the new scenario includes the presence of Distributed Power Generating Systems (DPGSs) that can inject locally energy into the grid. Moreover, the performances increase, combined with the costs reduction of solid state devices, has led to the development and the diffusion of the power converters with the result that, today, almost the totality of the electrical energy is controlled by power electronic systems.

The study of DPGSs is of a great interest from the point of view of the overall system, where it is important to choice where it is convenient to insert the DPGS [1], as well as from the point of view of the local system where there are problems to control and synchronization [2], [3]. A common way to find the optimal location of DPGSs is to minimize the power losses of the system through power flow algorithms as this is in general not sufficient. As the DPGSs are based on renewable source, sun or wind for example, their controllability is one of the main drawbacks. If these systems are not well controlled, their connection to the grid can lead to instability or failure. Besides, the capability of DPGSs to run under short grid disturbances is stressful by the existing standard for interconnecting these systems and so both synchronization algorithm and current controller became very important.

The goal of this chapter is to investigate a scenario, shown in figure 3.1, composed by a Smart Transformer (ST) [4], some loads and some DPGSs directly connected to the low voltage side of the ST.

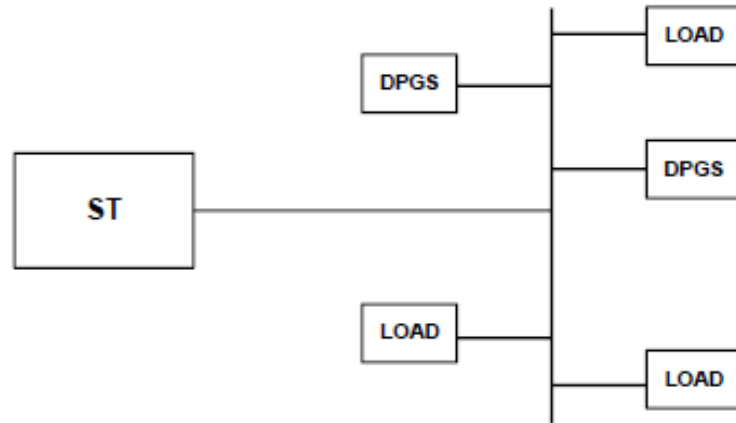


Fig 3.1 System structure

The ST is a Solid State Transformer (SST) used in electric distribution system to provide ac bus voltages with a fixed amplitude and frequency for each of the possible loads configuration. It can replace the traditional 50/60 Hz transformer by means of a high frequency isolated AC-AC transformer and power converters and for that it can be composed by one or more energy conversion stages, i.e. one or more power converters. The common drawback of its lower efficiency compared to the tradition transformer is becoming less evident due to the development of new power conversion architectures and power devices and so its new functionalities, such as to enhance the power quality, to protect from load disturbances, transient and voltage sags and to be robust and fault-tolerant, makes very attractive the study of a system with a ST.

On the other side, the correct analysis of the system requires that the loads and the DPGSs are properly modeled. In February 2010 CIGRE established working group C4.605: “Modelling and aggregation of loads in flexible power networks” [5]. This group has identified current international industry practice on load modeling for static and dynamic power system studies. The figure 3.2 shows the results for steady state power system studies.

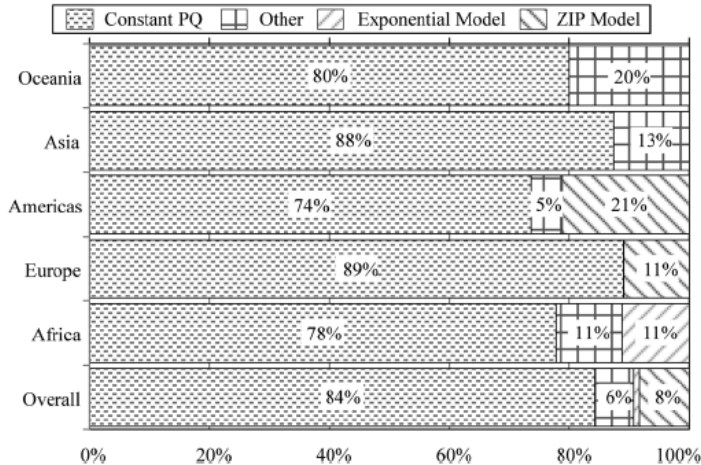


Fig 3.2 Load models used for steady state power system studies

As it can be seen, the most used is a constant power load (CPL) model, about 84%. This important result is justified by the consideration that power converters and motor drives, when well regulated, behave as constant power loads. A CPL example is a dc/ac inverter which drives an electric motor and tightly regulates the speed when the rotating load has a one-to-one torque–speed characteristic.

The main characteristic of a CPL is to have a current decrease when its voltage increases and vice versa and, so, it presents negative impedance for the small signal analysis that can impact the system stability. The impact of a CPL can be considered in a situation where also others kinds of loads that behave as a conventional positive load are present [6] – [9]. This kind of situation leads the system to have a stable and unstable region based on the ratio between positive and negative loads and so, choosing properly this ratio, the system is going to work in the stable region. This condition is less and less common due to the increasing diffusion of DPGs, whose model from the point of view of the ST is a negative load [5].

A critical scenario with only CPLs, the worst case for the stability, is now very attractive and for that is analyzed in this chapter with the aim to verify if it is possible to use controllers usually designed for stable systems, Proportional and P+Resonant described in the chapter 1, even when the system is unstable or if it is necessary to have a stable system to use them. This is very interesting for companies like

ABB Solar Group as they widely implement these controllers on their systems.

The schematic three-phase system representation is shown in the figure 3.3. It is composed by a Voltage Source Inverter (VSI) plus a LC filter representing the output stage of the ST, a DC-source representing the DC bulk of the ST, the CPL, the controller and the Pulse Width Modulator (PWM).

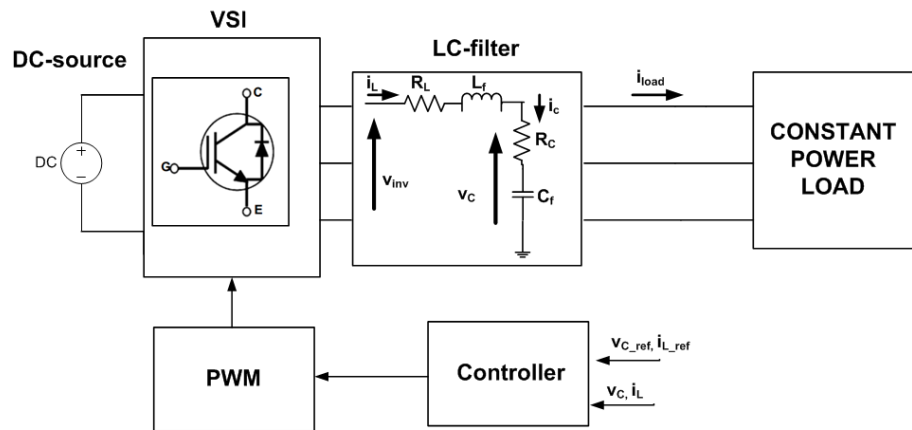


Fig 3.3 Schematic system representation

3.1 Constant power load characteristic and single loop control analysis

The figure 3.4 shows the i-v characteristic and the small signal behavior of a CPL with unity power factor.

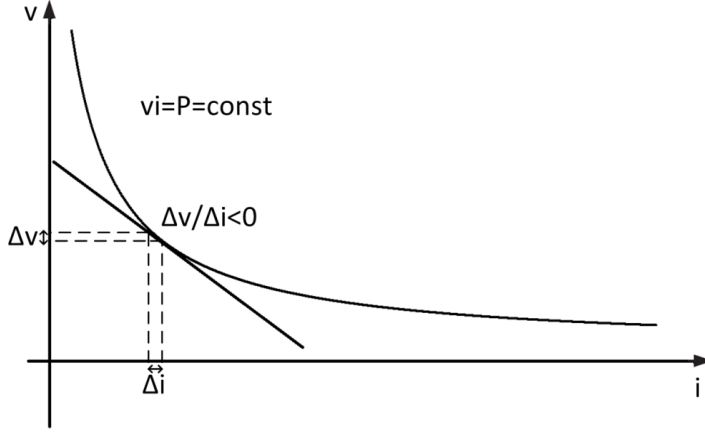


Fig 3.4 CPL i-v characteristic

For a load with unity power factor, the voltage and current are in phase and so the mathematic behavior can be described considering that the average power is constant for a constant power load as shown in the equation (3.1), where the second order term ($\Delta v_{\max} \Delta i_{\max}$) has been neglected as in the small signal analysis the current and voltage perturbation can be considered small [6]:

$$\begin{aligned}
 P_{CPL} &= \frac{1}{2} (V_{\max} + \Delta v_{\max}) (I_{\max} + \Delta i_{\max}) = \frac{1}{2} V_{\max} I_{\max} \Rightarrow \\
 \Rightarrow \frac{1}{2} (V_{\max} I_{\max} + V_{\max} \Delta i_{\max} + I_{\max} \Delta v_{\max} + \Delta v_{\max} \Delta i_{\max}) &= \frac{1}{2} V_{\max} I_{\max} \Rightarrow \quad (3.1) \\
 \Rightarrow \frac{\Delta v_{\max}}{\Delta i_{\max}} &= -\frac{V_{\max}}{I_{\max}} = -\frac{V_{rms}^2}{P_{CPL}} = -R_{CPL}
 \end{aligned}$$

This equation highlights that, even if the instantaneous resistance value is always positive ($V/I > 0$), the incremental resistance is always negative ($dV/dI < 0$) and, so, feeding CPLs can impact the system stability.

It is worth noting that a real CPL has a behavior as negative impedance only in a specific frequency range but it assumes that this range is included in the range for the control design.

The figure 3.5 shows the equivalent phase single loop control block diagram for one phase.

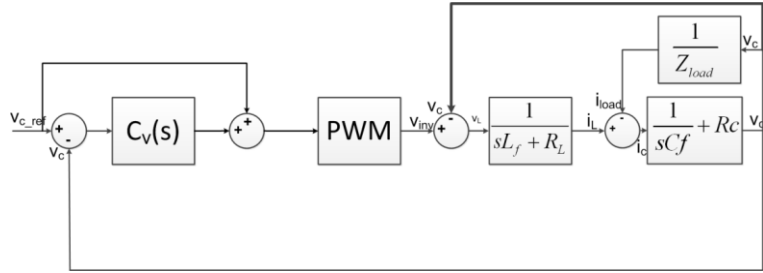


Fig. 3.5 Equivalent single phase single loop control block diagram

The control design is usually performed by means the open loop gain transfer function that is the product of the control transfer function, $C_v(s)$ and the plant transfer function. In this case, looking at the figure 3.5, the plant is:

$$\frac{v_c(s)}{v_{inv}(s)} = \frac{b_1 s + b_0}{a_2 s^2 + a_1 s + a_0}$$

$$\begin{aligned} b_1 &= C_f R_{CPL} R_c \\ b_0 &= -R_{CPL} \\ a_2 &= -C_f L_f R_{CPL} + C_f L_f R_c \\ a_1 &= L_f - C_f R_{CPL} R_L + C_f R_c R_L - C_f R_c R_{CPL} \\ a_0 &= R_L - R_{CPL} \end{aligned} \quad (3.2)$$

The plant is generally a stable system as it has only left half plane poles but, with the negative resistance introduced by the CPL, this is not always true: the plant could have also right half plane poles and be an unstable system. It depends by the specific value of the R_{CPL} that means how much the power is and by the specific values of the LC filter.

The following three phase system is analyzed:

- $S=1\text{MVA}$; $V_{\text{rms}}=230\text{V}$; $R_{CPL}=-0.158\Omega$; $f=50\text{Hz}$

The system components that have a high impact on the stability are the filter capacitor C_f , the filter inductor L_f and the passive damping resistor R_c . The variation effect of these 3 components on the system stability is analyzed.

The figure 3.6 shows the effect of the filter capacitor C_f . In this figure, the plant poles are calculated with $R_c=0.15\text{pu}$, $L_f=0.01\text{pu}$ and C_f varying in the range $[0.01\text{pu}-0.15\text{pu}]$ with a step of 0.005pu . As it can be seen, increasing the C_f value, the poles shift towards the left half plane and, so, the system tends to become stable. For these values, the system is stable when $C_f > 0.06\text{pu}$.

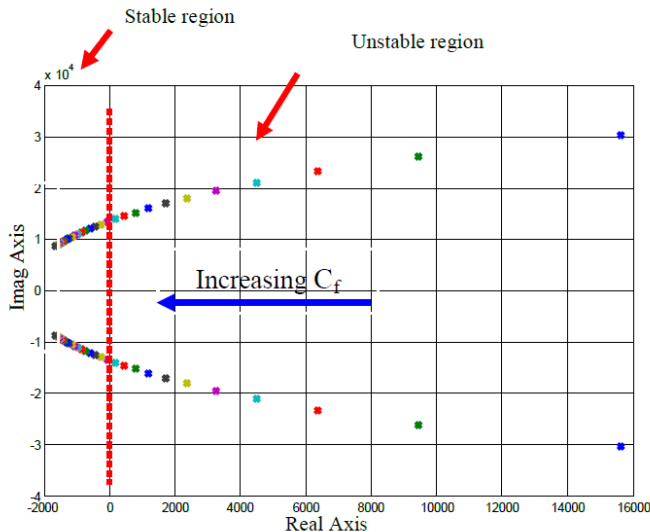
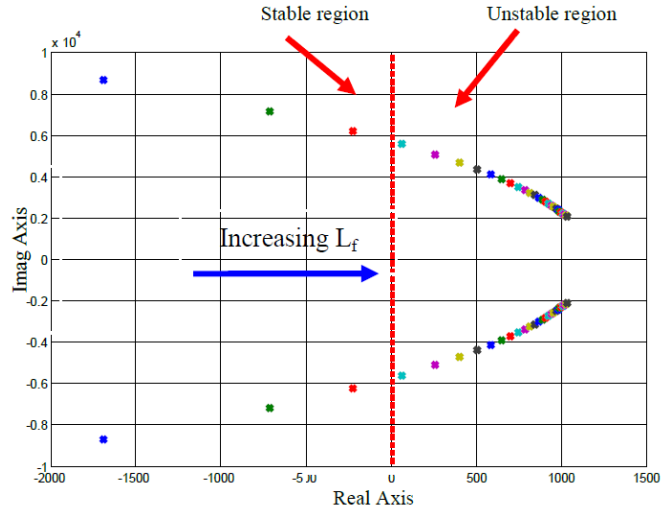
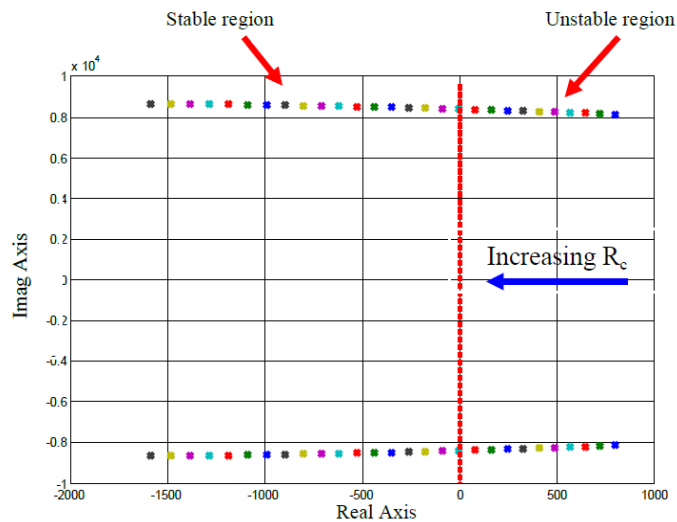


Fig 3.6 Effect of the filter capacitor C_f on the stability system

The figure 3.7 shows the effect of the filter inductor L_f . In this figure, the plant poles are calculated with $R_c=0.15\text{pu}$, $C_f=0.15\text{pu}$ and L_f varying in the range $[0.01\text{pu}-0.15\text{pu}]$ with a step of 0.005pu . As it can be seen, increasing the L_f value, the poles shift towards the right half plane and, so, the system tends to become unstable. For these values, the system is unstable when $L_f > 0.02\text{pu}$.

Fig 3.7 Effect of the filter inductor L_f on the stability system

The figure 3.8 shows the effect of the damping resistor R_c . In this figure, the plant poles are calculated with $L_f=0.01\text{pu}$, $C_f=0.15\text{pu}$ and R_f varying in the range $[0.01\text{pu}-0.15\text{pu}]$ with a step of 0.005pu . As it can be seen, increasing the R_c value, the poles shift towards the left half plane and, so, the system tends to become stable. For these values, the system is stable when $R_c > 0.06\text{pu}$.

Fig 3.8 Effect of the damping resistor R_c on the stability system

Considering a resonance frequency $f_r=1.3\text{kHz}$, the controller design is performed, in the alpha-beta frame with a P+Resonant control, in the two extreme conditions:

- 1) $\{C_f=0.15\text{pu}, L_f=0.01\text{pu}, R_c=0.15\text{pu}\}$ in which the plant is stable (Condition 1)
- 2) $\{C_f=0.01\text{pu}, L_f=0.15\text{pu}, R_c=0.01\text{pu}\}$ in which the plant is unstable. (Condition 2)

Indeed, the poles in the first condition are $p_{1,2}=(-1.69e3\pm 8.67e3i)\text{rad/s}$ and in the second are: $p_1=2.95e4\text{rad/s}$ and $p_2=2267\text{rad/s}$.

The simulation results are performed with Simulink® implementing the block diagram of figure 3.5. The constant power load has been implemented, exploiting the alpha-beta power theory, through the following equations:

$$\begin{aligned} i_{\alpha\text{CPL}} &= \frac{P_{\text{CPL}} V_{\alpha\text{CPL}}}{V_{\alpha\text{CPL}}^2 + V_{\beta\text{CPL}}^2} \\ i_{\beta\text{CPL}} &= \frac{P_{\text{CPL}} V_{\beta\text{CPL}}}{V_{\alpha\text{CPL}}^2 + V_{\beta\text{CPL}}^2} \end{aligned} \quad (3.3)$$

The PWM has been modeled as a delay, τ , considering the II order of the Pade' approximation:

$$R(s) = \frac{1 - \frac{\tau}{2}s + \frac{\tau^2}{12}s^2}{1 + \frac{\tau}{2}s + \frac{\tau^2}{12}s^2} \quad (3.4)$$

The delay τ has been chosen equal to $1.5/f_{\text{sw}}$ with a switching frequency, f_{sw} , equal to 5kHz , having considered $0.5/f_{\text{sw}}$ for the PWM and $1/f_{\text{sw}}$ for the computation time.

The P+ Resonant controller transfer function $C_v(s)$ is:

$$C_v(s) = k_{vp} + \frac{2k_{vi}\omega_{cut} s}{s^2 + 2\omega_{cut} s + \omega_o^2} \quad (3.5)$$

The choice of the control parameters does not present any specific problems when the system is stable. Hence, for the first condition, when the system is stable, they are:

- $\omega_o = 2\pi f = 2\pi 50 = 314.159 \text{ rad/s}$
- $\omega_{cut} = 8 \text{ rad/s}$
- $k_{vi} = 15 \text{ rad/s}$ to ensure a small steady-state error @ 50Hz
- $k_{vp} = 0.1$ to have a sufficient phase margin

The simulation results, in these conditions, are shown in the figures 3.9-3.12.

As it can be seen, the system works in the proper way because the load voltages are symmetrical, balanced and sinusoidal; the load power is 1MW and the errors are very small.

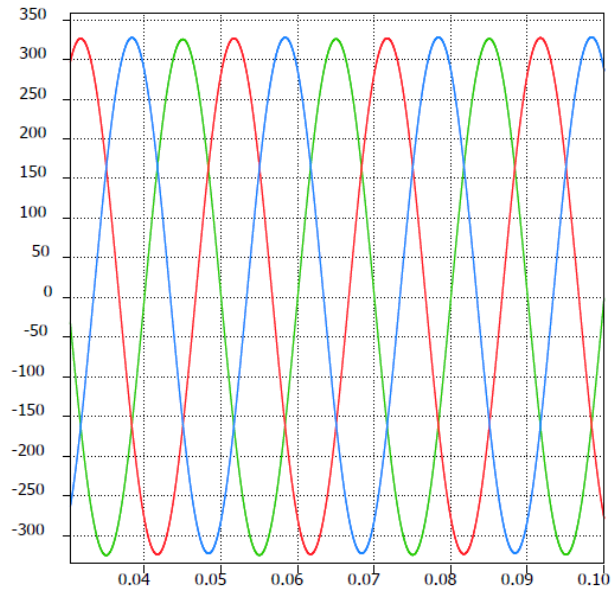


Fig 3.9 Load voltages

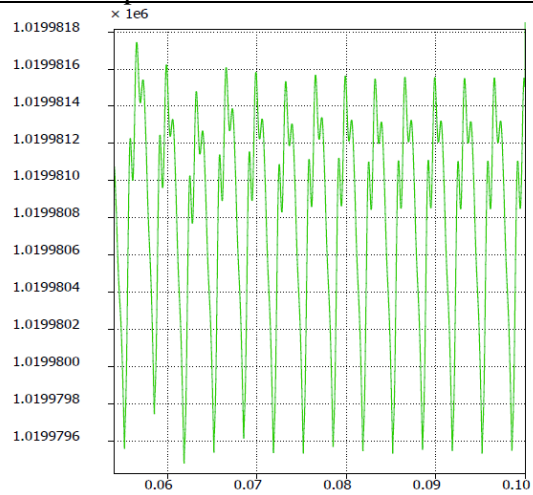


Fig 3.10 Load power

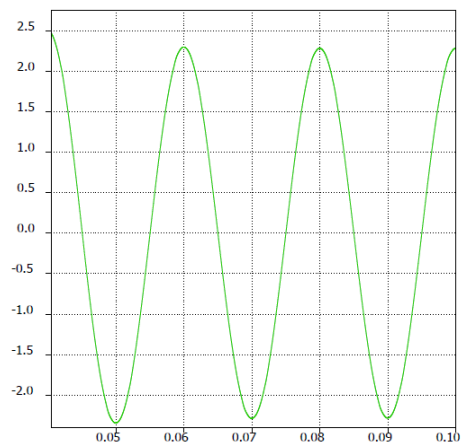


Fig 3.11 Alpha component error

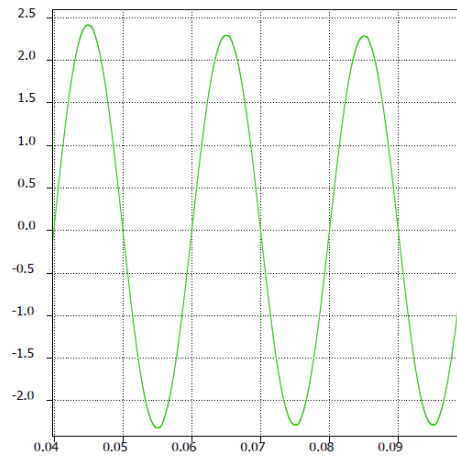


Fig 3.12 Beta component error

In the second condition, when the system is unstable with $\{C_f=0.01\text{pu}, L_f=0.15\text{pu}, R_C=0.01\text{pu}\}$, the controller design is performed through the root locus of the open loop gain, $G_v(s)C_v(s)$, with the SISO Toolbox® of MATLAB®. The same PWM delay of the previous case has been considered with the second-order of the Pade' approximation.

Starting with the same transfer function $C_v(s)$, with the same parameters:

- $\omega_o=2\pi f=2\pi 50=314.159 \text{ rad/s}$
- $\omega_{\text{cut}}=8 \text{ rad/s}$
- $k_{vi}=15\text{rad/s}$
- $k_{vp}=0.1$

in the figures 3.13 and 3.14 the root locus of the open loop gain is shown where the magenta markers are the closed loop poles of the system.

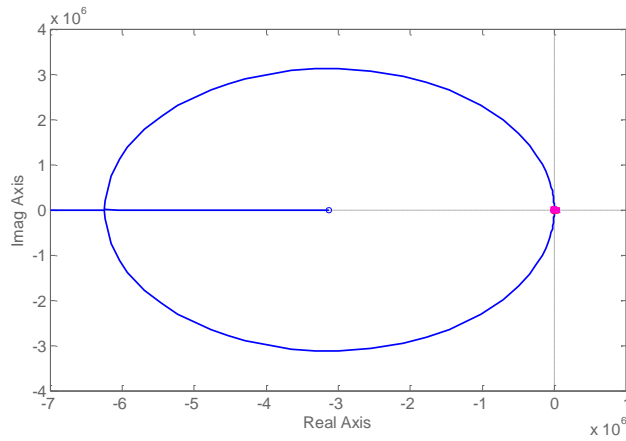


Fig 3.13 Open loop gain root locus

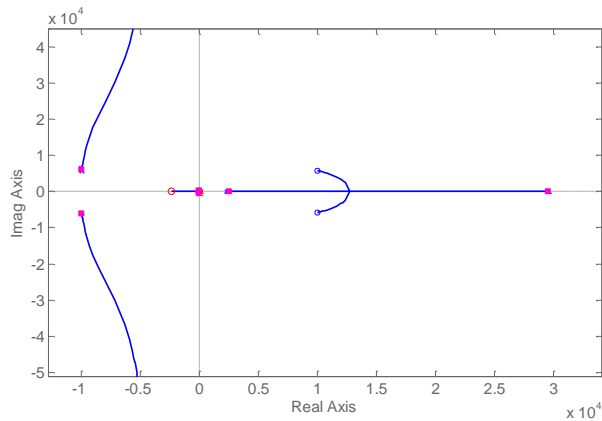


Fig 3.14 Zoom of the open loop gain root locus close to the imaginary axis

As it can be seen, it is not possible to stabilize the system with this kind of controller.

Hence, it can be concluded that only with a stable plant it is possible to feed the load in the correct way with a single loop using the P+Resonant controller and, to verify this condition, the CPL needs an appropriate selection of the passive components to have all left half plane poles. From the equation (3.2), for the Routh criterion, this condition is verified when the coefficients a_0 , a_1 and a_2 have the same sign:

$$\begin{aligned}
a_0 &= R_L - R_{CPL} \\
a_1 &= L_f - C_f R_L R_{CPL} + C_f R_L R_C - C_f R_c R_{CPL} \\
a_2 &= -C_f L_f R_{CPL} + C_f L_f R_C
\end{aligned} \tag{3.6}$$

Due to the physical feasibility only the sign minus is considered as R_L in a_0 is the parasitic resistance of the filter inductor and so a_0 has a negative value for the real cases:

$$\left. \begin{aligned}
a_0 &= R_L - R_{CPL} < 0 \\
a_1 &= L_f - C_f R_L R_{CPL} + C_f R_L R_C - C_f R_c R_{CPL} < 0 \\
a_2 &= -C_f L_f R_{CPL} + C_f L_f R_C < 0
\end{aligned} \right\} \Rightarrow$$

$$\left\{ \begin{aligned}
R_{CPL} &> R_L \\
R_{CPL} &> R_C \\
R_{CPL} &> \frac{L_f}{C_f (R_C + R_L)} + R_L \parallel R_c
\end{aligned} \right. \tag{3.7}$$

The first 2 conditions of the (3.7) are usually ensured as R_L and R_c are very small being the parasitic resistance of the filter inductor and the damping resistor while the last condition must be ensured to have a stable system. As it is possible to note, to stabilize the system the filter capacitor and the damping resistor must be increased and the filter inductor must be decreased in order to ensure this condition, as verified from the previous analysis.

In the next section, the double loop control will be analyzed to determine if it is possible to consider a LC filter that makes the system unstable and then make the system stable by the control action.

3.2 Double loop control analysis

The figure 3.15 shows the equivalent phase double loop control block diagram.

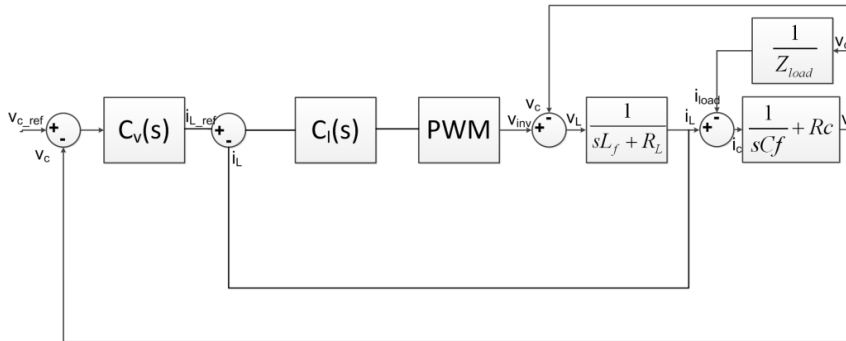


Fig 3.15 Equivalent single phase double loop control block diagram

Considering the same system of the previous section:

- $S=1\text{MVA}$; $V_{\text{rms}}=230\text{V}$; $R_{\text{CPL}}=-0.158\Omega$; $f=50\text{Hz}$

under the abovementioned two conditions:

- 1) $\{C_f=0.15\text{pu}, L_f=0.01\text{pu}, R_C=0.15\text{pu}\}$ (Condition 1)
- 2) $\{C_f=0.01\text{pu}, L_f=0.15\text{pu}, R_C=0.01\text{pu}\}$ (Condition 2)

The controller design is performed with a Proportional Current controller and a P+Resonant voltage controller looking at figure 3.15. In this case, there is a plant for the inner current control loop and a plant for the outer voltage control loop.

The plant for the inner current control loop is:

$$\frac{i_L(s)}{v_{inv}(s)} = G_i(s) = \frac{b_1 s + b_0}{a_2 s^2 + a_1 s + a_0}$$

$$b_1 = -C_f R_{CPL} + C_f R_c$$

$$b_0 = 1 \quad (3.8)$$

$$a_2 = -C_f L_f R_{CPL} + C_f L_f R_c$$

$$a_1 = L_f - C_f R_L R_{CPL} + C_f R_L R_c - C_f R_c R_{CPL}$$

$$a_0 = R_L - R_{CPL}$$

The poles, of course, are the same of the single control loop while it is present a right half plane zero $z_1=2475\text{rad/s}$.

For this plant, with $\{C_f=0.15\text{pu}, L_f=0.01\text{pu}, R_c=0.15\text{pu}\}$, the proportional gain of the current controller has been selected in order to have a more damped system for the outer loop [10], [11]:

$$C_I(s) = k_{ip} = 40 \quad (3.9)$$

The plant for the outer voltage loop is:

$$G_v(s) = Z_c \frac{G_i(s)C_I(s)}{1 + G_i(s)C_I(s)} \quad (3.10)$$

The poles are $p_1=-8.006\text{e}6\text{rad/s}$ and $p_2=2463\text{rad/s}$.

The right half plane pole of the (3.10) cannot be eliminated with the control action, changing the k_{ip} value, since it depends by the right half plane zero in $G_i(s)$ introduced by the constant power load.

The PWM has been modeled as a delay, $\tau=300\mu\text{s}$, considering the II order of the Pade' approximation, as for the single loop analysis.

The P+Resonant voltage controller design is performed through the root locus of the open loop gain, $G_v(s)C_v(s)$, with the SISO Toolbox® of MATLAB®. Starting with following parameters of $C_v(s)$:

- $\omega_o=2\pi f=2\pi 50=314.159\text{rad/s}$
- $\omega_{cut}=8\text{ rad/s}$
- $k_{vi}=15\text{ rad/s}$
- $k_{vp}=0.1$

The root locus of the open loop gain is shown in the figures 3.16 and 3.17, where the magenta markers are the closed loop poles of the system.

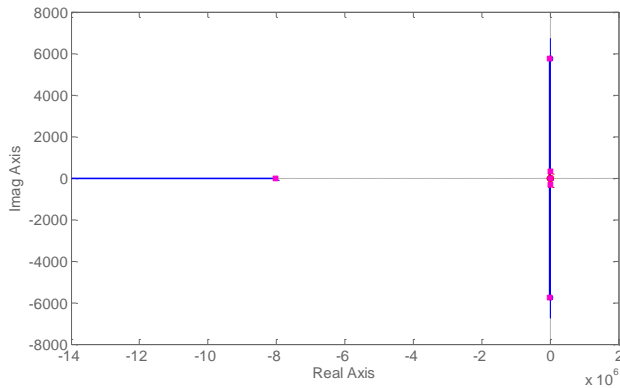


Fig 3.16 Open loop gain root locus

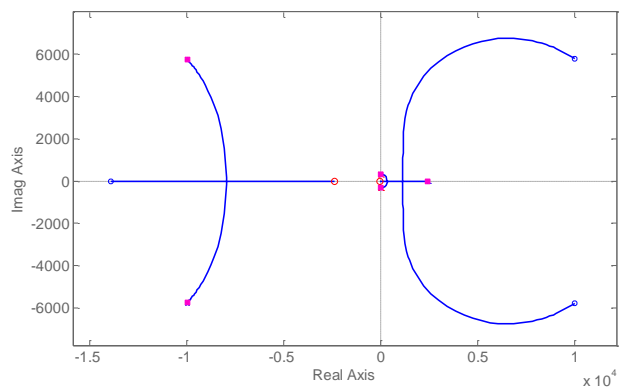


Fig 3.17 Zoom of the open loop gain root locus close to the imaginary axis

As it can be seen, it is not possible to stabilize the system with this kind of controller. In the second condition, with $\{C_f=0.01\text{pu}, L_f=0.15\text{pu}, R_C=0.01\text{pu}\}$, the plants for the inner current control loop and the outer control loop are unstable because both have a right half plane. The control design will not be performed because it leads to the same consideration of the single control loop. Hence, it can be concluded that, with the double loop control, it is not possible to stabilize the system making not possible to feed a constant power load using the Proportional and the P+Resonant controls. A single loop is necessary to continue using these standard and well-known controllers.

References

- [1] C. Wang, M.H. Nehrir, "Analytical approaches for optimal placement of distributed generation sources in power systems", IEEE Transactions on Power Systems, vol. 19, no. 4, pp.2068-2076, Nov. 2004.
- [2] F. Blaabjerg, E. Teodorescu, M. Liserre, A.V. Timbus, "Overview of Control and Grid Synchronization for Distributed Power Generation Systems", IEEE Transactions on Industrial Electronics, vol. 53, no. 5, pp.1398,1409, Oct. 2006.
- [3] A.Timbus, M. Liserre, R. Teodorescu, F. Blaabjerg, "Synchronization methods for three phase distributed power generation systems - An overview and evaluation", IEEE 36th Power Electronics Specialists Conference (PESC '05), pp.2474-2481, 16 June 2005.
- [4] G. Quartarone, M. Liserre, F. Fuchs, N. Anglani, G. Buticchi, "Impact of the modularity on the efficiency of Smart Transformer solutions", 40th Annual Conference of the IEEE Industrial Electronics Society (IECON 2014), pp.1512-1518, Oct. 29 2014-Nov. 1 2014.
- [5] J. V. Milanovic, K. Yamashita, S. Martinez Villanueva, S.Z. Djokic, L.M. Korunovic, "International Industry Practice on Power System Load Modeling", IEEE Transactions on Power Systems, vol.28, no.3, pp.3038-3046, Aug. 2013.
- [6] A. Emadi, "Modeling of power electronic loads in AC distribution systems using the generalized State-space averaging method", IEEE Transactions on Industrial Electronics, vol.51, no.5, pp.992-1000, Oct. 2004.
- [7] A. Emadi, A. Khaligh, C.H. Rivetta, G.A. Williamson, "Constant power loads and negative impedance instability in automotive systems: definition, modeling, stability, and control of power

electronic converters and motor drives", IEEE Transactions on Vehicular Technology, vol.55, no.4, pp.1112-1125, July 2006.

- [8] D. P. Ariyasinghe, D.M. Vilathgamuwa, "Stability analysis of microgrids with constant power loads", IEEE International Conference on Sustainable Energy Technologies (ICSET 2008), pp.279-284, 24-27 Nov. 2008.
- [9] D. M. Vilathgamuwa, X.N. Zhang, S.D.G. Jayasinghe, B.S. Bhangu, C.J. Gajanayake, King Jet Tseng, "Virtual resistance based active damping solution for constant power instability in AC microgrids," 37th Annual Conference on IEEE Industrial Electronics Society (IECON 2011), pp.3646-3651, 7-10 Nov. 2011.
- [10] Poh Chiang Loh, D.G. Holmes, "Analysis of multiloop control strategies for LC/CL/LCL-filtered voltage-source and current-source inverters," IEEE Transactions on Industry Applications, vol.41, no.2, pp.644-654, March-April 2005.
- [11] Yun Wei Li, "Control and Resonance Damping of Voltage-Source and Current-Source Converters With LC Filters," IEEE Transactions on Industrial Electronics, vol.56, no.5, pp.1511-1521, May 2009.

Chapter 4

Minimum Computing MPPT

The wide interest for Maximum Power Point Tracking (MPPT) control is justified by the attempt to maximize the energy harvested from photovoltaic sources in all the operating conditions. Several control techniques can be adopted [1]-[10], both analog and digital, to achieve good MPPT efficiency. Digital techniques are best suited to implement adaptive control. The runtime optimization of MPPT digital control is in the focus of many studies, mostly regarding the Perturb&Observe (P&O) technique described in the chapter 1. The two parameters determining the MPPT efficiency and the tracking speed P&O technique are the sampling period T_{MPPT} and the duty-cycle step perturbation magnitude ΔD .

There are a lot of techniques to select these 2 parameters. For example:

- ΔD is updated based on the sampled ratio $\Delta I/\Delta D$ and T_{MPPT} is consequently set as smaller as ΔD decreases [1].
- A fuzzy technique is adopted to select ΔD , considering both the power and current variations ΔP and ΔI [2].
- ΔD is corrected based on $\Delta P/\Delta V$ ratio [3].
- ΔD is set proportional to ΔP [4], [5].

The previous techniques involve a continuous update of ΔD which can lead to temporary P&O swing around the MPP with oscillations across more than 3 operating points. A simplified approach using two ΔD values, a big one to improve MPP tracking capabilities when sun irradiance is rapidly varying, and a small one adopted for steady operation can be adopted [6]. The use of two ΔD values only does not guarantee maximum energy harvesting in all operating conditions. In [7] the duty perturbation ΔD is set as smaller as the panel voltage is closer to the theoretical MPP. Such approach needs a preliminary modeling of the PV source and cannot guarantee high MPPT

efficiency. In [8] some adaptive MPPT methods are overviewed and a technique is proposed wherein the convergence to optimum MPPT is driven by an exponential adaptation law. In [9] the power variation ΔP is used as error signal to correct the duty-cycle reference by means of PI compensation. In [10] an FPGA controller is discussed wherein the optimal sampling period T_{MPPT} setup is achieved based on a system response estimation done through FFT. The level of MPPT efficiency achievable by the techniques mentioned above is conditioned by many factors, such as the modeling assumptions, the duty-cycle and sampling period correction law adopted and the computing capabilities of the digital device adopted for the control implementation. To this regard, all of them involve a variable amount of computations, including the calculation of the ratios (e.g. $\Delta I/\Delta D$, $\Delta P/\Delta V$) used as figure of merit, the subsequent calculations required by the adaptation law and the additional calculations required by specific estimation/decision algorithm used. As a consequence, many methods and algorithms yield high MPPT efficiency at the price of high computing effort, which is not compatible with low cost requirements. This issue is stressed in applications where a single digital device is wanted to perform multiple control functions, such as, for example, the LED lighting systems fed by PV sources [11], eventually including an energy storage device. In such situations, different dc-dc converters are involved in the source-side regulation and in the load-side regulation, and a single device must control the MPPT converter, the dimmable LED converter and the bulk voltage to manage the storage device status. More in general, achieving maximum energy harvesting with minimum cost devices is a fundamental renewable energy industry demand.

The method presented realizes the real time adaptation of a photovoltaic P&O MPPT control with minimum computing effort to maximize the PV energy harvesting against changes of sun irradiation, the temperature and the characteristics of the PV source and by the overall system the PV source is part of. It exploits the correlation existing among the MPPT efficiency and the onset of a permanent 3 levels quantized oscillation around the MPP that is the steady-state condition for the algorithm. Like in [12], the method detects this steady-state condition and, based on that, changes the MPPT parameters. A comparison between the proposed method and the one

presented in [12] will be done through PSIM[®] simulations to set exactly the same test conditions.

As a multi-function control application case study, a TMS320F28035 Texas Instruments Piccolo[™] Microcontroller (μc) is used to implement the adaptive PV MPPT control algorithm, the LED driver dimming control and the bulk voltage control of a 70W LED lighting system prototype fed by a photovoltaic source with a capacitor working as storage device. The choice of the F28035 μc is carried out to use the same family, the TI C2000, that *ABB Solar Group* implements on its converters but with a single-core system as the goal of the proposed method is the minimum computing effort. Hence the aim of this chapter is to determine an optimize MPPT algorithm that can be implemented in the ABB Solar Group systems.

4.1 Light-to-Light system case study

The figure 4.1 shows the block diagram of the system under study. It is composed by a PV panel, a LED array, a boost dc–dc converter for the MPPT of the PV panel and a buck dc–dc converter for driving the LEDs array.

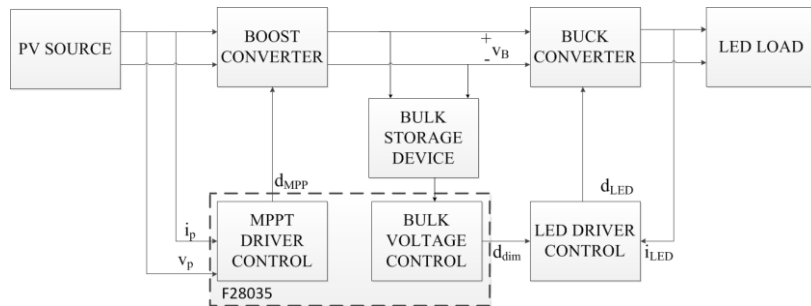


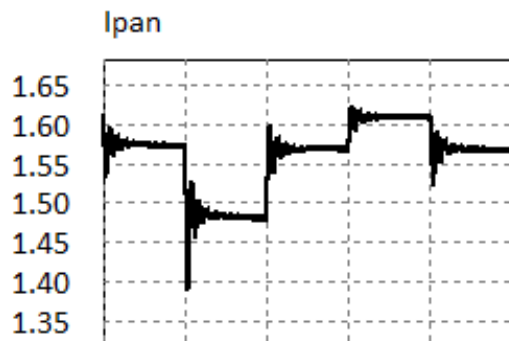
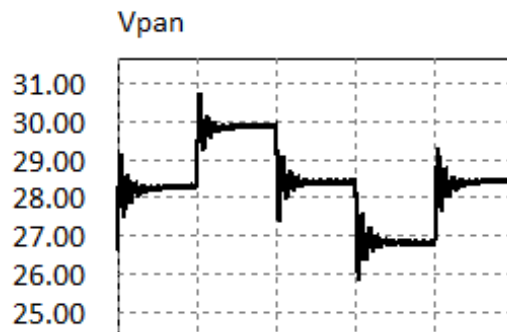
Fig. 4.1 Light to Light System

The global system control goal is to harvest the maximum PV energy to feed a dimmable LEDs array. Energy storage and loads dimming is an effective mean to implement intelligent energy management solutions [11] when energy generated by renewable sources is involved. In fact, photovoltaic inverters with storage and load management capabilities are highly appealing today. To this regard, the block diagram of the figure 4.1 can be considered as a general system concept, as the LEDs array can be replaced by any kind of dimmable load and the storage device can be a capacitor, a super capacitor or a battery. The overall control algorithm modulates the bulk voltage to balance the instant power between the PV source and the LEDs array through the storage device charge and discharge, while modulates the LEDs array dimming to balance the instant power between the PV source and the storage device when its voltage or current exceeds the allowed operating ranges. The LEDs array is driven by a hysteretic controller ensuring constant current operation and using an enable command to dimm the driver.

The P&O technique is still today the simplest and cheapest mean to achieve photovoltaic MPPT. Indeed, the dramatic fall of microcontrollers cost helps in implementing quite inexpensive MPPT controllers. The energy harvesting effectiveness of P&O depends on sampling period and step perturbation magnitude setup [13]. MPPT high dynamic promptness is required to fastly track rapidly changing irradiation conditions, while small oscillations around the MPP are required in steady state conditions. These two conditions are conflicting for MPPT setup, as energy harvesting is improved by large magnitude step perturbations in the former and minimum step perturbations in the latter. The adaptive methods for perturbative MPPT controls try to achieve a tradeoff in the setup of the perturbation magnitude by means of adaptation laws based on the elaboration of sampled voltage, current, power and duty-cycle. The effectiveness of such approaches is heavily conditioned by modeling assumptions and by the type of adaptation law, mostly based on gain and shift factors and algorithms whose optimal setup just lifts the problem to a different layer. However, there is a universal property of P&O technique allowing achieving easy optimal MPPT setup.

4.2 Adaptive duty-cycle setup

The figure 4.2 shows the voltage, current and power of a PV panel operating with a P&O MPPT controller based on Open-Loop (OL-MPPT) cycle-by-cycle duty-cycle step perturbation $\Delta D[k]$. A correct P&O MPPT steady-state operation involves a 3 points oscillation across the MPP as shown in the figure 4.2 (a), (b) and (c).



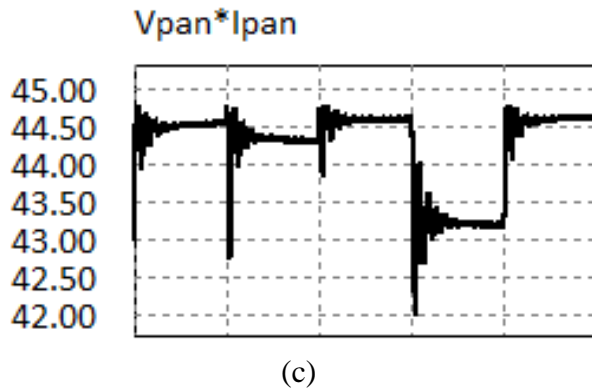


Fig. 4.2. Open-Loop P&O MPPT 3 points operation with $T_{MPPT}=10\text{ms}$.

The smaller the duty-cycle step perturbation ΔD , the higher the energy harvested cycle-by-cycle in steady state [13]. In theory, the best would be to drop $\Delta D[k]$ magnitude at the minimum value allowed by the microcontroller used to implement the MPPT control. Regarding the sampling period T_{MPPT} , we also get energy harvesting benefits in reducing it [13] in dynamic irradiance conditions. However, the sign of duty-cycle perturbation for $k+1$ -th cycle, $\text{sign}(\Delta D[k+1])$, is based on the sign of power variation, $\text{sign}(\Delta P[k])$, at the end of the k -th cycle. The combined effect of irradiance variations, voltage and current measurement errors, quantization, poorly damped system transients, sampling period shortness and too small $\Delta D[k+1]$ can lead the operation of the P&O MPPT controller into a four, or more, points oscillations around the MPP, as shown in the figure 4.3 (a), (b) and (c). In this case the system works in an unpredictable way, not ensuring maximum energy harvesting.

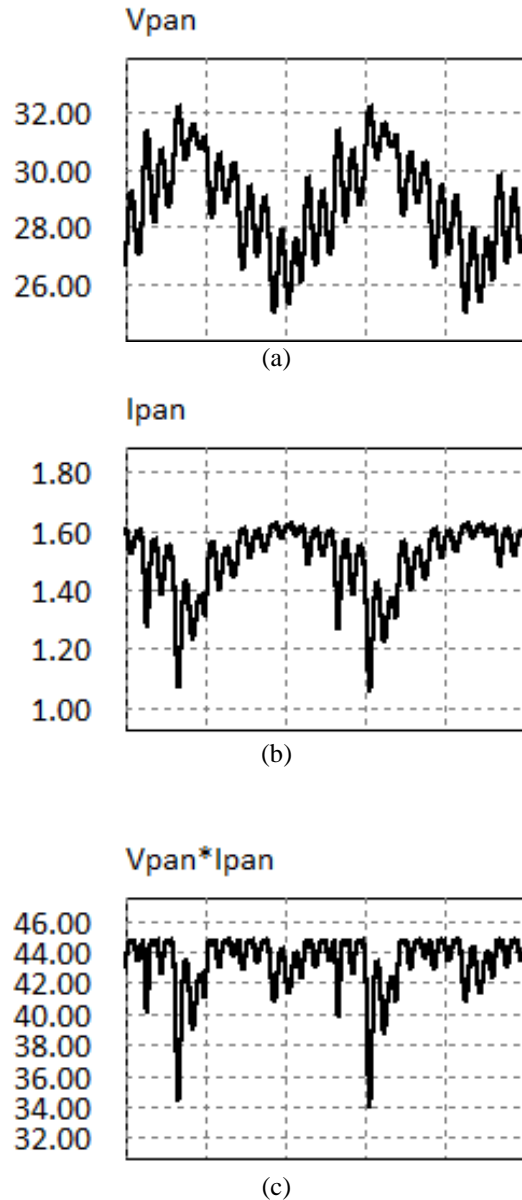


Fig. 4.3 Open-Loop P&O MPPT 4 points operation with $T_{MPPT}=2\text{ms}$.

The adaptive MPPT method proposed is based on a simple concept: the maximum energy harvesting is achieved, in whatever irradiance condition, when the minimum duty-cycle step perturbation ΔD and the minimum sampling period T_{MPPT} magnitudes ensuring a 3

points MPPT operation are detected. Such search can be easily implemented by means of the counters-based algorithm illustrated in the block diagram of the figure 4.4. The `main_counter` is updated each sampling period: it swings between 0 and 1, cycle-by-cycle, if the MPPT control is running a 3 points operation; it exceeds 1 only when 3 points operation is missed. The `n_counter` is incremented every time the `main_counter` sets to 1. If `n_counter` reaches a given value N_n , then ΔD is decreased of a value $\Delta\Delta D$. Thus, if the 3 points operation persists for a sufficient time, ΔD is decreased to increase the energy harvesting. The `p_counter`, instead, is increased every time the `main_counter` sets to a value greater than 1. If the `p_counter` reaches a given value N_p , then ΔD is increased of a value $\Delta\Delta D$. Thus, if the 3 points operation is missed for a sufficient long time, ΔD is increased to increase the energy harvesting. The sampling period T_{MPPT} does not need to be updated too frequently, as its main impact is on the tracking speed capabilities when the irradiation changes are fast (windy cloudy days). It is sufficient that it is not lower than the settling time of the panel voltage response after each ΔD step perturbation.

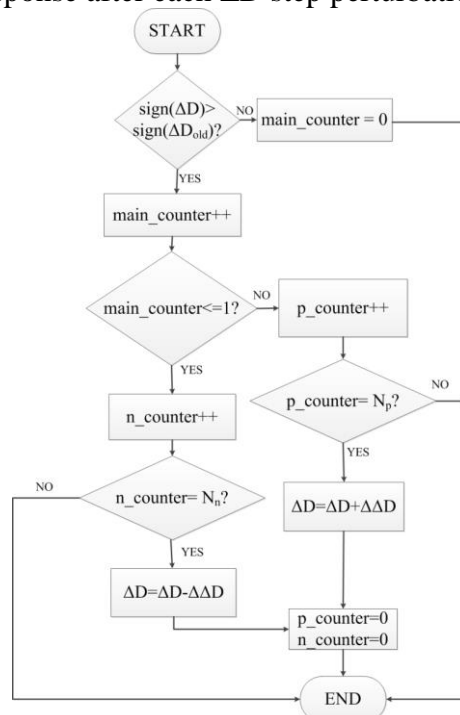


Fig. 4.4 ΔD adaptive setup for 3 point MPPT operation

In [12], the detection of the 3 points operation is done comparing the output of the MPPT algorithm at the k -th cycle and at $(k-1)$ -th cycle to identify if the output exhibits a rising edge, $F(k)=1$, or a falling edge, $F(k)=0$. The last 4 flanks are stored in a vector $F_v = [F(k), F(k-1), F(k-2), F(k-3)]$ and if the vector F_v has two consecutive flanks of the same value, $[1,1]$ or $[0,0]$, the system is working under a 3 points MPPT operation.

A system with a PV panel, a boost DC/DC converter and a battery has been considered to compare the presented methods, MPPT_Counter and the one presented in [12], MPPT_Flanks, in term of energy harvesting and has been simulated in PSIM[®] to ensure exactly the same test conditions. The figure 4.5 shows the circuit representation of that system with a Norton-based equivalent representation of the PV panel, with the same numerical values of [11] for the boost converter and the PV panel and with a battery of 48V.

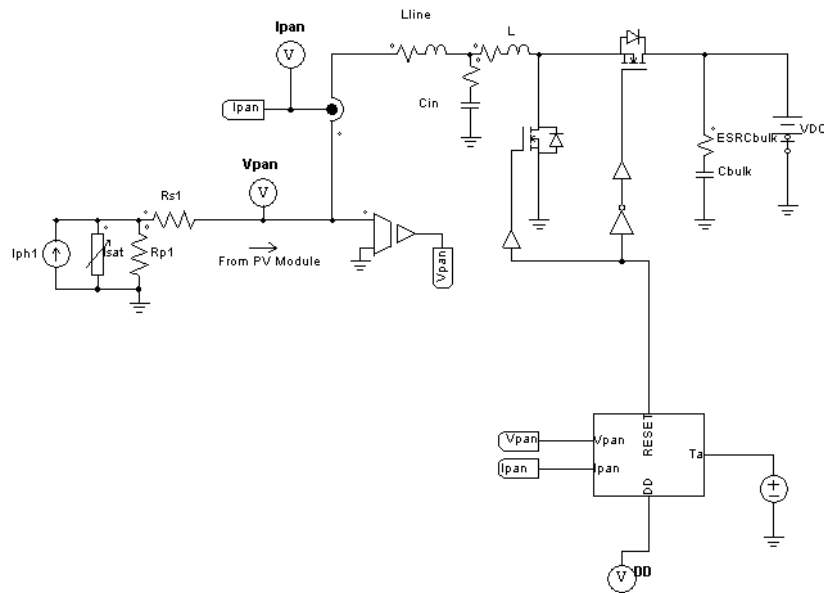


Fig. 4.5 Circuit representation

The figures 4.6-4.9 show the simulation results in terms of panel voltage, panel current, power extracted for a solar irradiation level $S=1000\text{W/m}^2$ and ΔD . Without loss of generality, to work in the same

conditions, N_n and N_p have been set equal to 1 and the same $\Delta\Delta D$ has been considered for both methods. As it is possible to note from the figures, the 2 algorithms lead to the same results in term of energy harvesting as the average power is 215.64W for the MPPT_Counter and 215.48W for the MPPT_Flanks. The difference between the 2 methods consists in how the 3 points operation is detected, 2 counters or a vector and the possibility to relax the variation of ΔD through the values N_n and N_p for the MPPT_Counter. Hence the MPPT_Counter has a slightly simpler implementation through the counters and allows reducing, with N_n , the ΔD value only when the 3 points operation is regularly established and achieving, with N_p , a fast tracking in presence of fast irradiance variations.

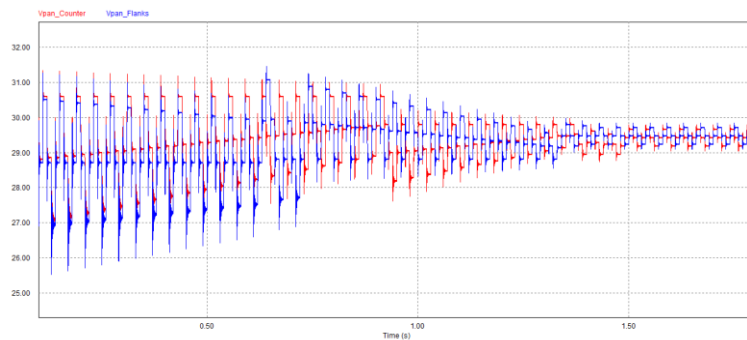


Fig. 4.6 Panel Voltage

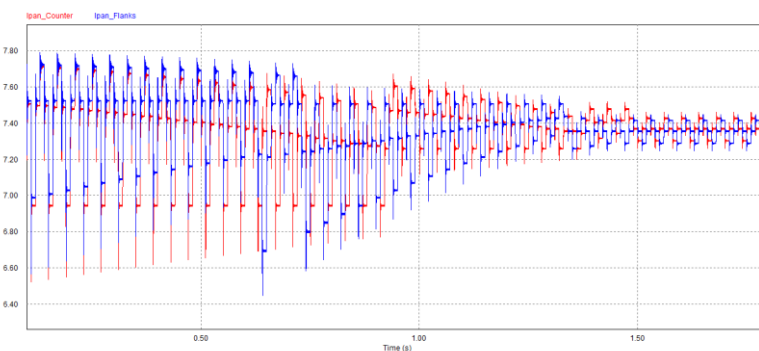


Fig. 4.7 Panel Current

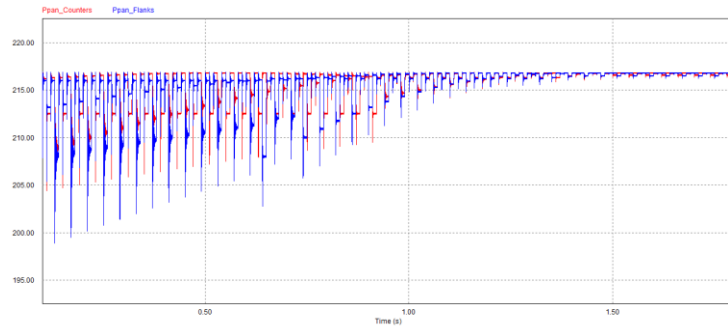
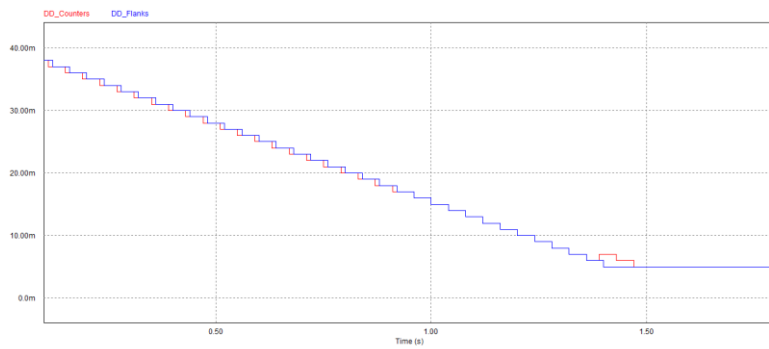


Fig. 4.8 Panel Power

Fig. 4.9 ΔD variation

The transfer function $G_{vp,d} = \hat{v}_p / \hat{d}_{MPP}$ determines the panel voltage step response in OL-MPPT, where \hat{v}_p is the panel voltage perturbation and \hat{d}_{MPP} is the duty-cycle perturbation. In the system of the figure 4.1, the OL-MPPT is implemented with a boost convert, so that:

$$G_{vp,d} = -\frac{V_B}{1 + G_p L_p s + L_p C_p s^2} \quad (4.1)$$

where L_p is the inductance, C_p is the capacitance, G_p is the PV panel conductance and V_B is the dc bulk voltage. According to (4.1), the panel voltage response to ΔD step perturbation settles to its final value with absolute error $|\varepsilon|$ within the time:

$$T_\varepsilon = \frac{2}{G_p} \sqrt{\frac{C_p}{L_p}} \ln(|\varepsilon|/2) \quad (4.2)$$

The values of L_p and C_p are known from boost power stage design. The value of G_p can be determined run-time from the samples of panel voltage and current acquired for MPPT control.

4.3 LED Dimming-based Bulk Voltage regulation

Thanks to low computing needs of adaptive MPPT described in previous section, a single microcontroller can be used to implement the other control functions needed by a system like the one shown in the figure 4.1. As illustrated, the aim of that system is to ensure maximum energy harvesting from the PV source and adequate power balance among the PV source, the load and the storage device. This multiple tasks can be implemented through an adequate dynamic control of the bulk voltage v_B . The design of compensation network for Bulk Voltage Control (BVC) can be realized based on the dynamic model of the system, treated in [11], where analog BVC was discussed and experimented.

The control signal generated by the BVC loop modulates the dimming duty-cycle D_{dim} of the LED driver, as shown in the figure 4.1. The dimming frequency f_{dim} must be much smaller than the switching frequency f_{LED} , to avoid flickering of LEDs light. For the case under study, it is $f_{dim}=3kHz$ and $f_{LED}=400kHz$.

The uncompensated BVC loop gain of the system in the figure 4.1 is given by (4.3):

$$G_{B,D_{dim}}(s) = \frac{\hat{v}_B}{\hat{d}_{dim}} \Big|_{\hat{d}_{mpp}=0} = G_{B0} \frac{b_0 + b_1 s + b_2 s^2}{a_0 + a_1 s + a_2 s^2 + a_3 s^3} \quad (4.3)$$

where

$$\begin{aligned} D'_{mpp} &= I - D_{mpp}; \quad G_{B0} = G_{led} G_{pwm} V_B; & G_{led} &= -V_F I_F / V_B^2 \\ a_0 &= G_p D_{mpp}^2 + D_{dim} G_{led} & b_0 &= 1 \\ a_1 &= C_b + C_p D_{mpp}^2 + L_p G_p D_{dim} G_{led} & b_1 &= G_p L_p \\ a_2 &= L_p (C_b G_p + C_p D_{dim} G_{led}) & b_2 &= C_p L_p \\ a_3 &= L_p C_b C_p \end{aligned}$$

In [11], it is shown that the compensated BVC loop gain crossover frequency f_c must be sufficiently low to avoid LED light flickering which occur if the BVC tries to compensate the bulk voltage oscillations determined by the MPPT control, whose equivalent frequency is $f_{mppi} = 1/(4T_{MPPT})$. A type II compensation is then sufficient:

$$G_{D_{dim},B}(s) = \frac{\hat{d}_{dim}}{\hat{v}_B} = \frac{\omega_0}{s} \frac{1 + s/\omega_Z}{1 + s/\omega_P} \quad (4.4)$$

Considered the sampling period setup discussed in the previous section, the equivalent MPPT frequency range is $[1/(4T_{MPPTmax}), 1/(4T_{MPPTmin})] = [25\text{Hz}, 125\text{Hz}]$. A 2Hz crossover frequency f_c is selected, with 65° phase margin ϕ_m to design the compensator (4.4), accounting for phase lag effects of the A/D sampling. The compensator (4.4) indeed is implemented in digital form by means of the Backward Euler analog-to-digital transform (4.5):

$$s = f_{dim}[1 - z^{-1}] \Rightarrow G_{D_{dim},B}(z) = \frac{B_0 + B_1 z^{-1}}{1 + A_1 z^{-1} + A_2 z^{-2}} \quad (4.5)$$

leading to the difference equation (4.6):

$$y[k] = B_0x[k] - B_1x[k-1] + A_1[k-1] - A_2y[k-2] \quad (4.6)$$

The Bode plot of the uncompensated BVC loop gain for the example under study is shown in the figure 4.10. The closed-loop gain $G_{B,D_{mppt}} = \hat{v}_B / \hat{d}_{mppt}$ provides the response of the bulk voltage to P&O OL-MPPT step-wise duty-cycle perturbations.

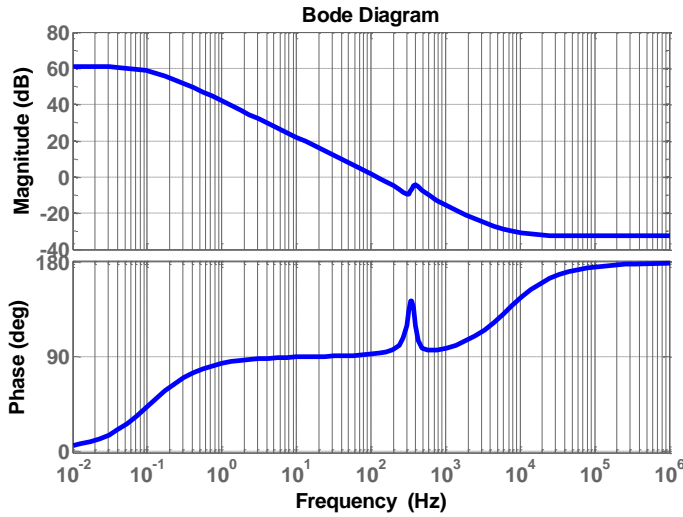


Fig. 4.10 Bode diagram of CtB

Its Bode plot is shown in the figure 4.11 for values of solar irradiation S from $50W/m^2$ to $1000W/m^2$ with $50W/m^2$ step.

The figure 4.11 shows that the flat region of $G_{B,D_{mppt}} = \hat{v}_B / \hat{d}_{mppt}$ gain in the frequency range [2Hz, 200Hz] contains the MPPT frequency range [25Hz, 125Hz]: this prevents load flickering.

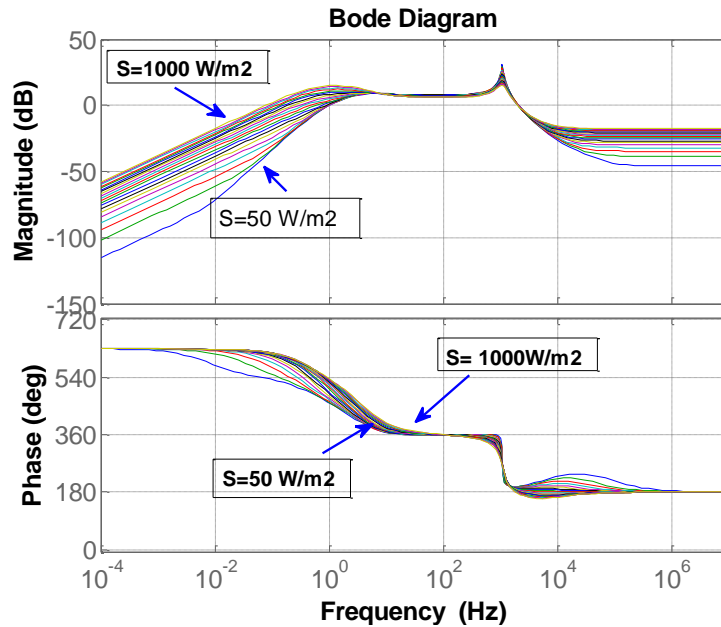


Fig. 4.11 Bode diagram of Duty-to-Bulk Voltage gain at different level of solar irradiation

4.4 Experimental results

The case study system of the figure 4.1 is composed by:

- a KYOCERA KC120-1 PV panel, with $P_{MPP} = 120 \text{ W}$, $V_{MPP} = 16.9 \text{ V}$, $I_{MPP} = 7.1 \text{ A}$, $V_{OC} = 21.5 \text{ V}$, $I_{SC} = 7.45 \text{ A}$
- a string of 10 Diamond Dragon LUW W5AP LEDs in series with $V_F = 3.5 \text{ V}$ and $I_F = 1.5 \text{ A}$
- a Texas Instruments LM3409HV Constant OFF time LED driver with DC/DC step down converter
- a 32-bit Texas Instruments TMS320F28035 Piccolo™ Microcontroller

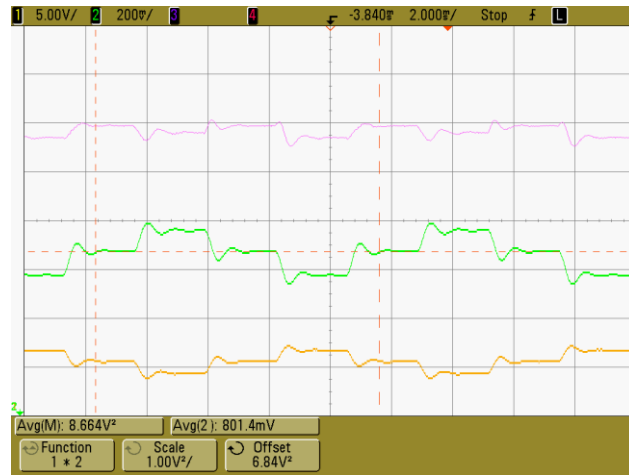
The F28035 μc implements the overall control of the Light-to-Light system of the figure 4.1. The ΔD and T_{MPPT} adaptation is run within the MPPT interrupt. The value of $\Delta\Delta D$ was set to the minimal

possible value allowed by the F28035 μc , which corresponds to a signal tick:

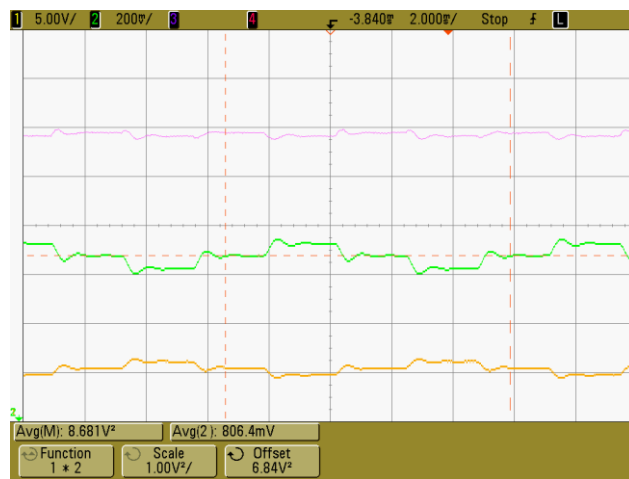
$$\Delta\Delta D \text{ min} = \frac{f_{CLK}}{f_{PWM}} 100 = \frac{60kHz}{60MHz} 100 = 0.1\% \quad (4.7)$$

The values of N_n and N_p thresholds have been fixed at 120 and 5, respectively. The high N_n value is justified by the need to reduce the duty-cycle step magnitude ΔD only when a 3 points operation is regularly established. The small N_p value is justified by the need to achieve a fast tracking in presence of fast irradiance variations. ΔD is also subjected to an upper limit to avoid large oscillations around the MPP. The sampling period T_{MPPT} resolution is 0.1ms. Starting from nominal $T_{MPPT} = 10\text{ms}$, the F28035 μc realizes a low frequency periodic T_{MPPT} adaptation, according to the differential PV instant panel conductance G_p .

The figures 4.12 and 4.13 show the experimental measurements of panel voltage, current and power, in low and high irradiance conditions, without and with adapted ΔD , for a fixed sampling period value T_{MPPT} . The power waveforms show lower magnitude oscillations as a consequence of the ΔD adaptation. The figures 4.14 and 4.15 show the effects of T_{MPPT} adaptation. In this case, no improvement is expected about the energy harvesting efficiency; rather, it is evident that the next perturbation of OL-MPPT acts suddenly after the panel voltage settles. The performances of the BVC have been validated too.

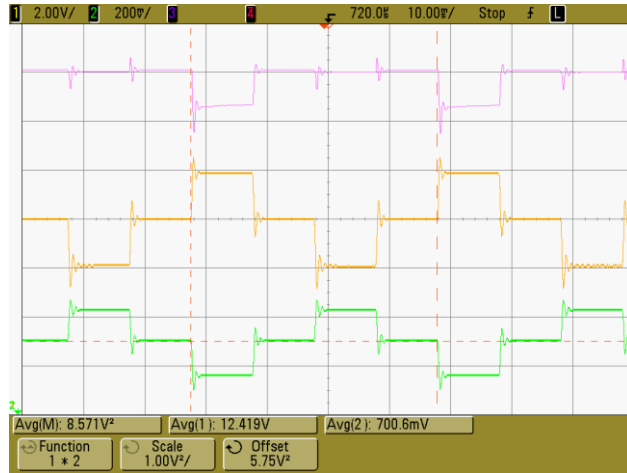


(a)



(b)

Fig. 4.12 Low irradiance operation: (a) not adapted ΔD , (b) adapted ΔD

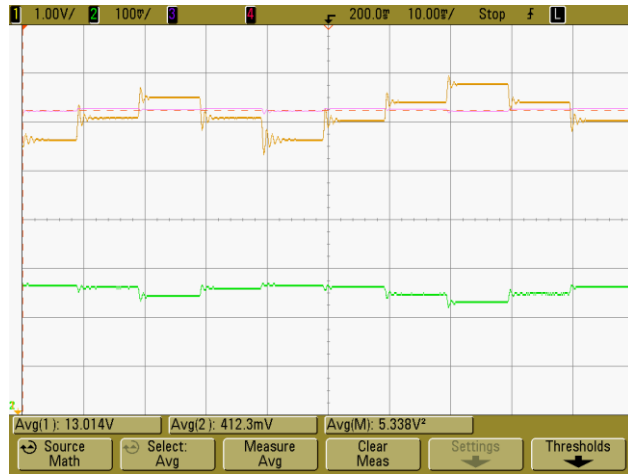


(a)

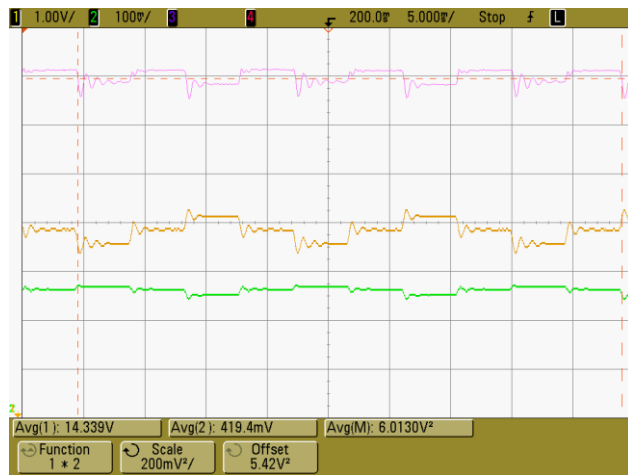


(b)

Fig. 4.13 High irradiance operation: (a) not adapted ΔD , (b) adapted ΔD

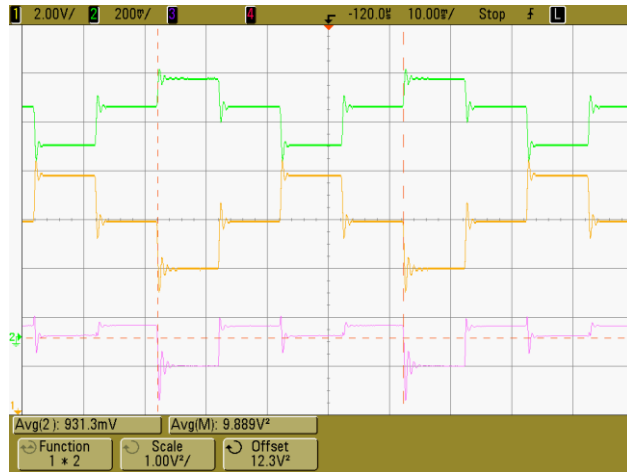


(a)



(b)

Fig. 4.14 Low-irradiance operation (a) fixed $T_{MPPT}=10\text{ms}$ (b) adapted $T_{MPPT}=2\text{ms}$



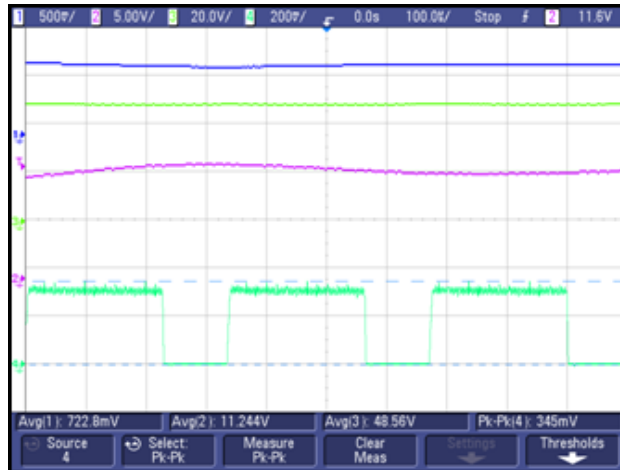
(a)



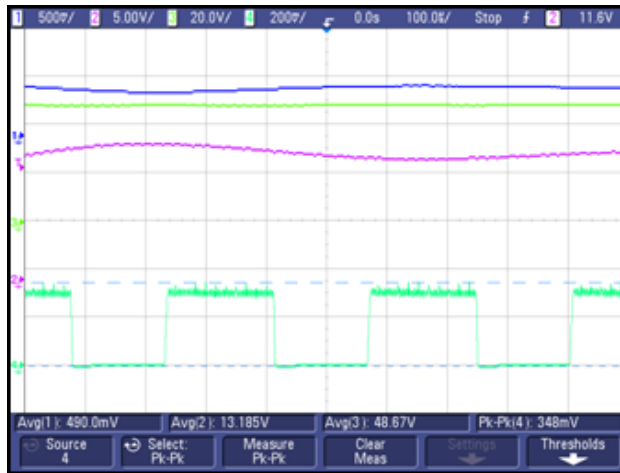
(b)

Fig. 4.15 High-irradiance operation: (a) fixed $T_{MPPT}=10\text{ms}$ (b) adapted $T_{MPPT}=2\text{ms}$

In the figure 4.16 the effect of the voltage regulation on the LED current is shown for two different irradiance conditions. The LED current waveform reflects the duty-cycle of the dimming signal, which is modulated by the BVC: the higher the irradiance level, the higher power delivered to the LED.



(a)



(b)

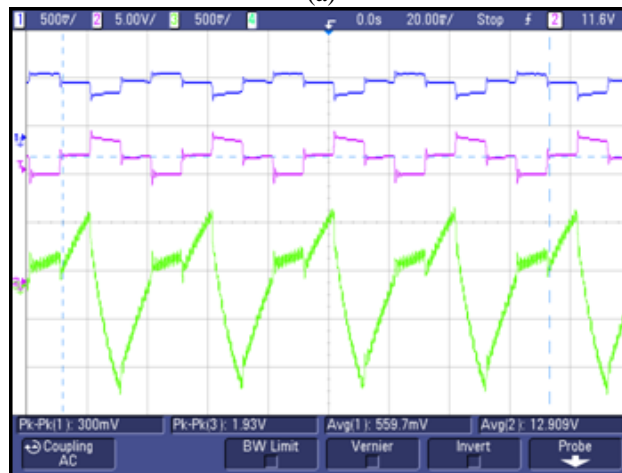
Fig. 4.16 Effect of the voltage regulation on the LED current (light blue), (a) high irradiance level and (b) medium irradiance level.

The figure 4.17(a) shows the PV voltage and current oscillation obtained with the optimized values of the MPPT parameters while the bulk voltage is regulated around the reference value of 48V. The figure 4.17(b) shows the effect of the MPPT perturbation at the bulk

voltage. As expected, the bulk capacitor absorbs the power fluctuation coming from the PV side, the bulk voltage follows the MPPT oscillations and the power delivered to the LED remains constant. An important outcome of such operation mode is an improvement of the P&O OL-MPPT energy harvesting capabilities. In fact, when the output voltage of the dc-dc converter used to implement the MPPT is tightly regulated, namely it is almost constant; each step-up ΔD perturbation involves a step-down variation on the panel voltage only, and vice-versa. Instead, if the output voltage of the dc-dc converter is allowed to swing, following the step-wise ΔD perturbation, it happens that each step-up ΔD perturbation involves as a step-down variation on the panel voltage as a step-up in the output converter voltage. In this way, for whatever ΔD magnitude, the oscillations on the panel voltage will be reduced with respect to the case of tightly regulated output voltage. The previous discussion highlights that, in case the storage device is a battery, it has to be interfaced with the bulk by means of a power converter allowing free swing of the bulk voltage at the MPPT frequency, if true maximum PV energy harvesting is desired. In other words, it is not the best for true maximum PV energy harvesting operation if the output of the dc-dc converter implementing the P&O OL-MPPT is terminated onto a device involving, or requiring, a tightly regulated voltage.



(a)



(b)

Fig. 4.17 Panel Voltage (blue), Panel Current (violet), Bulk Voltage (green) and LED current (light blue) in normal operating condition

References

- [1] Yuncong Jiang; Qahouq, J.A.A.; Haskew, T.A., "Adaptive Step Size With Adaptive-Perturbation-Frequency Digital MPPT Controller for a Single-Sensor Photovoltaic Solar System", *IEEE Transactions on Power Electronics*, vol.28, no.7, pp.3195,3205, July 2013.
- [2] Mohd Zainuri, M.A.A.; Mohd Radzi, M.A.; Soh, A.C.; Rahim, N.A., "Adaptive P&O-fuzzy control MPPT for PV boost dc-dc converter", *IEEE International Conference on Power and Energy (PECon)*, pp.524,529, 2-5 Dec. 2012.
- [3] Al-Diab, A.; Sourkounis, C., "Variable step size P&O MPPT algorithm for PV systems", *12th International Conference on Optimization of Electrical and Electronic Equipment (OPTIM)*, pp.1097,1102, 20-22 May 2010.
- [4] Khaehintung, N.; Wiangtong, T.; Sirisuk, P., "FPGA Implementation of MPPT Using Variable Step-Size P&O Algorithm for PV Applications", *International Symposium on Communications and Information Technologies (ISCIT '06)*, pp.212,215, Oct. 18 2006-Sept. 20 2006.
- [5] Weidong Xiao; Dunford, W.G., "A modified adaptive hill climbing MPPT method for photovoltaic power systems", *IEEE 35th Annual Power Electronics Specialists Conference (PESC '04)*, pp.1957,1963 Vol.3, 20-25 June 2004.
- [6] Chao Zhang; Dean Zhao; Jinjing Wang; Guichang Chen, "A modified MPPT method with variable perturbation step for photovoltaic system", *IEEE 6th International Power Electronics and Motion Control Conference (IPEMC '09)*, pp.2096,2099, 17-20 May 2009.
- [7] Piegari, L.; Rizzo, R., "Adaptive perturb and observe algorithm for photovoltaic maximum power point tracking", *Renewable Power Generation (IET)*, vol.4, no.4, pp.317,328, July 2010.

- [8] Buyukdegirmenci, V.T.; Bazzi, A.M.; Krein, P.T., "A comparative study of an exponential adaptive perturb and observe algorithm and ripple correlation control for real-time optimization", IEEE 12th Workshop on Control and Modeling for Power Electronics (COMPEL), pp.1,8, 28-30 June 2010.
- [9] Abdelsalam, A.K.; Massoud, A.M.; Ahmed, S.; Enjeti, P., "High-Performance Adaptive Perturb and Observe MPPT Technique for Photovoltaic-Based Microgrids", IEEE Transactions on Power Electronics, vol.26, no.4, pp.1010,1021, April 2011.
- [10] P. Manganiello, M. Ricco, E. Monmasson, G. Petrone, G. Spagnuolo, "On-line optimization of the P&O MPPT method by means of the system identification," Industrial Electronics Society, 39th Annual Conference of the IEEE (IECON), pp.1786,1791, 10-13 Nov. 2013.
- [11] Femia, N.; Fortunato, M.; Vitelli, M., "Light-to-Light: PV-Fed LED Lighting Systems", IEEE Transactions on Power Electronics, vol.28, no.8, pp.4063,4073, Aug. 2013.
- [12] Saavedra-Montes, A.J.; Ramos-Paja, C.A., Trejos-Grisales, L.A. "Adaptive Maximum Power Point Tracking Algorithm for Multi-Variable Applications in Photovoltaic Arrays", Revista EIA, 10(20), pp. 209-222.
- [13] N. Femia, G. Petrone, G. Spagnuolo, M. Vitelli, Power Electronics and Control Techniques for Maximum Energy Harvesting in Photovoltaic Systems, CRC press, 2012

Conclusions

The aim of this thesis has been to investigate control issues in photovoltaic (PV) systems as the design of PV plants, in the present-day evolving scenario, is not completely defined. As the development of this work was born from cooperation between the *Power Electronics and Renewable Sources Laboratory* of the University of Salerno and the *ABB Solar Group* company (ex *Power-One*) of Terranuova Bracciolini (AR), Italy, the starting points have been highlighted from the industry but they have also a great impact on the scientific and technologic fields with the final goal to increase the performance of the PV systems at any level, system, grid and circuit.

At system level, an improved Dead-Beat (DB) control based on an Observe&Perturb (O&P) algorithm has been developed with the aim to have static and dynamic performance better than the widely used, also by *ABB Solar Group*, Proportional Integral (PI) control. The O&P idea is to perturb the system control laws of values ΔV_d and ΔV_q , at a fixed time step T_a , to get zero average tracking errors keeping the fast dynamic of the DB control. Bigger are the average errors and bigger are the perturbations ΔV_d and ΔV_q . General guideline for the selection of the parameters, T_a , ΔV_d and ΔV_q , have been provided making sure that they do not affect the system stability. As case study, a Neutral Point Clamped (NPC) inverter in the dq frame, based on the *ABB AURORA ULTRA* inverter, has been considered. A comparison between the PI, the DB, the Integral+DB (I+DB) and the O&P DB controls has been done through simulations performed by a dedicated C++ language tool. The simulation results, taking the inputs from a real case of the Indian grid, highlighted that the O&P DB has the same fast dynamic of the standard DB, faster than the PI and presents zero average tracking errors while the PI has zero average tracking errors, as expected, but slow dynamic. The DB and I+DB controls have dynamic faster than the PI but no zero average tracking errors. Hence the O&P DB control showed the best performance both static and dynamic. In presence of model mismatch, the O&P DB control still keeps zero average tracking errors but the dynamic start becoming slower. However, as shown in the simulation results, this mismatch has to be consistent, like no grid feedforward, to actually impact the

dynamic. Both O&P method and simulation tool are not only for NPC inverters but they are very general being able to be applied to all the converters. The O&P DB control has also been implemented on the F28379D Texas Instruments Microcontroller (μc) to test the feasibility of all its components, i.e. O&P algorithm, control and modulation on a single embedded system and the results from the tool simulations and the μc were the same making the O&P DB control suitable for digital systems. This μc implementation has been performed at the Texas Instruments of Freising, Germany.

At grid level, a critical scenario composed by a Smart Transformer (ST), some loads and some Distributed Power Generating Systems (DPGSs) directly connected to the low voltage side of the ST has been investigated. The correct analysis of the system requires that the loads and the DPGSs are properly modeled and the most used, for steady state power system studies, is a constant power load (CPL) model as power converters and motor drives, when well regulated, behave as constant power loads. The main characteristic of a CPL is to present negative impedance for the small signal analysis that can impact the system stability. The worst case for the stability is when the load presents only a CPL. Hence, a three-phase system with a Voltage Source Inverter (VSI), a LC filter representing the output stage of the ST, a DC-source representing the DC bulk of the ST, the CPL, the controller and the Pulse Width Modulator (PWM) has been analyzed. The aim has been to verify if it is possible to use controllers usually designed for stable systems, Proportional and P+Resonant, even when the system is unstable or if it is necessary to have a stable system to use them. This is very interesting for companies like *ABB Solar Group* as they widely implement these controllers on their systems. This investigation put the basis for all the future works for DPGSs with CPLs because it has been proved that it is not possible to use a double loop control, as the closed-loop system is always unstable, and that the system should be stable with the action of the LC filter, for a single loop control, to use these controllers as it is not possible to stabilize the system with them. The stability conditions have been provided and they mainly depend by the ratio $L_f/C_f R_c$ where L_f is the filter inductor, C_f the filter capacitor and R_c the damping resistor. This ratio should be less than the equivalent CPL resistance to have a stable system. The analysis of a system with a CPL has been developed also in

cooperation with the *Chair of Power Electronics* of the Albrechts-Universität zu Kiel, Germany.

At circuit level, a method to determine the sampling period T_{MPPT} and the duty-cycle step perturbation magnitude ΔD has been presented to optimize the existing methods to extract power from the PV source. This method realizes the real time adaptation of a photovoltaic P&O MPPT control with minimum computing effort to maximize the PV energy harvesting against changes of sun irradiation, the temperature, the characteristics of the PV source and by the overall system the PV source is part of. It has been exploited the correlation existing among the MPPT efficiency and the onset of a permanent 3 levels quantized oscillation around the MPP. Such universal property of P&O MPPT technique allows achieving optimum setup in microcontroller P&O MPPT implementation just by means of two counters, thus avoiding computations on measured quantities and the use of sophisticated models and algorithms. A comparison between an existing adaptive MPPT algorithm and the proposed one has highlighted that they have the same results in term of energy harvesting but the proposed one presents a slightly simpler implementation as the existing method uses a vector while the proposed one only 2 counters with the possibility to relax the ΔD adaptation through the 2 values N_n and N_p . As a multi-function control application case study, a F28035 Texas Instruments Microcontroller (μc) has been used to implement the adaptive PV MPPT control algorithm, the LED driver dimming control and the bulk voltage control of a 70W LED lighting system prototype fed by a photovoltaic source with a capacitor working as storage device. The experimental results showed the good performance of the proposed fully integrated control architecture, suitable for implementation with low cost microcontrollers. The proposed method can be applied to all the digital systems as it is not related to the specific implementation.

List of publications

- [1] M. De Cristofaro, N. Femia, M. Migliaro, G. Petrone, “Minimum Computing Adaptive MPPT Control”, International Symposium on Industrial Electronics (ISIE 2014), Istanbul, Turkey June 2014.
- [2] M. De Cristofaro, N. Femia, D. Toledo, W. Zamboni, “Residential Applications of PV-Systems with Energy Storage2.” European Power Conversion Intelligent Motion Conference (PCIM 2013) Nuremberg, Germany, May 2013
- [3] M. De Cristofaro, G. Di Capua, N. Femia, G. Petrone, G. Spagnuolo, D. Toledo, “Model and Methods for Energy Productivity Analysis of PV Systems”, International Conference on Industrial Informatics (INDIN 2015), Cambridge, UK, July 2015
- [4] G. Buticchi, G. De Carne, M. De Cristofaro, N. Femia, M. Liserre, G. Petrone, “The Effect of a Constant Power Load on the Stability of a Smart Transformer”, International Conference on Industrial Informatics (INDIN 2015), Cambridge, UK, July 2015

Acknowledgements

Il mio dottorato di ricerca è stato un percorso molto lungo, pieno di cambiamenti in corso d'opera ma proprio per questo mi ha permesso di crescere sia dal punto di vista professionale che umano.

Tutto questo non sarebbe stato possibile senza l'aiuto e il supporto dei miei tutor, i professori Nicola Femia e Giovanni Petrone. La loro presenza costante è stata determinante per portare a compimento questo percorso.

Grazie al Prof. Maurizio Longo, coordinatore del dottorato, che è stato una guida in tutti questi anni ed è sempre stato disponibile a sostenermi.

Grazie all'azienda ABB Solar Group (ex Power-One) di Terranuova Bracciolini (AR) per aver finanziato il dottorato e aver fornito gli input per lo studio e la ricerca effettuata.

Grazie al Prof. Marco Liserre dell'Università di Kiel per aver supportato la mia ricerca durante i sei mesi trascorsi con lui in Germania.

Grazie a Ulrike Behringer e Jan Pape, miei attuali manager alla Texas Instruments, a Uwe Mielkau, il mio manager precedente, e a tutto il mio team per avermi sostenuto ed aiutato negli ultimi due anni del mio dottorato.

Infine, grazie a tutta la mia famiglia e ai miei amici che danno un senso a tutto quello che faccio e a cui dedico questo lavoro.

A tutti voi, un grazie sincero ed appassionato.

Massimiliano.